Composites Part B 254 (2023) 110586

Contents lists available at ScienceDirect

Composites Part B

journal homepage: www.elsevier.com/locate/compositesb

Unified analysis for tailorable multi-scale fiber reinforced cementitious composites in tension

Peizhao Zhou, Peng Feng *

MOE Key Lab of Civil Engineering Safety and Durability, Department of Civil Engineering, Tsinghua University, Beijing, 100084, China

ARTICLE INFO

Handling Editor: Dr Hao Wang

Keywords:
Multi-scale fibrous reinforcement
Engineered cementitious composite
Ultra-high performance concrete
Tension stiffening
Modeling

ABSTRACT

Fibers applied to reinforce the cementitious matrix exhibit a wide range of scales, from distributed carbon nanomaterials, chopped short fibers to continuous fibrous reinforcements. When a cementitious matrix is jointly toughened by reinforcing fibers at multiple scales, Multi-Scale Fiber Reinforced Cementitious Composite (MSFRC) tailored built on the micromechanics-based approach and bond-slip mechanism is proposed in this study. The composite actions of MSFRC, namely, tension stiffening, ductility enhancing and synergetic effects, are explained within a universal perspective. In addition, a 1-D numerical model using spring elements is developed to simulate the tensile behavior of MSFRC based on the crack band theory, fiber-bridging model and Monte Carlo simulation. The scales, types and contents of reinforcing fibers, interface behavior and stochastic nature can be considered in the model. Finally, it is found that the predicted mechanical response and crack evolution process match well with the experimental results obtained from literatures.

1. Introduction

As one of the most dominant construction materials worldwide, cement-based materials exhibit post-peak tension-softening behavior described by crack band theory [1]. The cementitious matrix needs to be toughened by reinforcing materials in practical structural applications due to the low tensile strength and rapid crack propagation. Continuous fibrous reinforcements are applied to improve the load carrying capacity; the incorporation of chopped short fibers controls the cracking growth; the carbon nanomaterials refine the microstructure. To exploit the advantages of reinforcing fibers at different scales, the design strategy of Multi-scale Fiber Reinforced Cementitious Composite (MSFRC) is proposed in this paper, as illustrated in Fig. 1. By tailoring the characteristics of reinforcing fibers and mix composition, MSFRC can achieve the comprehensive utilization of reinforcing fibers to obtain the optimum mechanical performance.

As shown in Fig. 2, all reinforcing fibers can be classified into three forms based on the geometric scale: the distributed carbon nanomaterials (CNMs) at the microscopic scale, chopped short fibers at the mesoscopic scale and aligned continuous fibrous reinforcements (referred to as continuous fibers) at the macroscopic scale. Based on the fiber bridging and toughening at the micro- and mesoscopic scales [6–9], short fiber reinforced cementitious composites (SFRCs) indicate that the cementitious matrix is reinforced by CNMs or chopped short fibers, including carbon nanotube (CNT)/cement composites, engineering cementitious composites (ECC), ultra-high performance concrete (UHPC), recycled fiber reinforced concrete [10]. Another category is continuous fiber reinforced cementitious composites (CFRCs), e.g., reinforced concrete (RC), fiber reinforced polymer (FRP) textile reinforced cement (TRC).

For CFRC with a moderate reinforcement ratio, the composite actions, characterized by the tension stiffening effect, tension softening effect of concrete and bond deterioration, were defined and discussed [11]. In design and construction, if a considerable tensile load capacity of a CFRC member is needed, a high reinforcement ratio can be conducted accurately by constructional arrangements. However, it is known that wide cracks (generally from 0.2 mm to 4.6 mm) in CFRC members would form under overloading and cyclic-loading, which makes CFRC structures encounter the corrosion induced by the ingress of ions and performance degradations [12].

To improve the cracking resistance and energy absorption capacity, CNMs and chopped short fibers are applied to reinforce the cement-based material. SFRC with post-cracking tension-softening behavior, can be generally formed by reinforcing fibers at the micro- and mesoscopic scales with untailored physical properties. On the other hand, strain-hardening behavior accompanied by the formation of tightly distributed cracks can be achieved, in combination with a proper design

* Corresponding author.
E-mail addresses: zhoupz18@mails.tsinghua.edu.cn (P. Zhou), fengpeng@tsinghua.edu.cn (P. Feng).

https://doi.org/10.1016/j.compositesb.2023.110586
Received 5 July 2022; Received in revised form 25 January 2023; Accepted 1 February 2023
Available online 9 February 2023
1359-8368/

Nomenclature

A_r	area of a single continuous fiber
a, b	empirical parameters defining the slip at ultimate bond stress
c	radius of matrix flaw
c_f	bridging parameter
c_m	matrix cover
c_0	scale parameter of Weibull distribution of flaw size
c_{mc}	critical flaw size
c_{ckm}	the largest radius of the matrix flaws in the failure section
c_{ckf}	the largest radius of the composite flaws in the first cracking section
C_{clear}	clear distance between lugs
$erf(V_f)$	error function of fiber volume fraction
E_m, E_r, E_f	elastic modulus of the matrix, continuous and short fiber
f	snubbing coefficient
f'	fiber strength reduction
f_c	cylinder compressive strength of matrix
f_r	yield strength of steel or ultimate strength of FRP
f_{tk}	characteristic tensile strength of matrix
f_{tm}	average tensile strength of matrix
F_r	interface frictional force along the continuous fiber
F_f	normal resultant force of the interface friction along the short fibers
F_{pulley}	resultant pulley force at the end point of the inclined short fibers
$F(c)$	cumulative distribution function (CDF) of the matrix flaw size
g	snubbing factor
k	brittle coefficient
k_α, k_β	ascent and descent slopes of linear bond-slip relationship
K	confinement parameter
K_m, K_f	matrix and composite fracture toughness
l_r, l_f	minimum crack spacing of continuous and short fiber reinforced cementitious composites
l_r', l_f'	transmission length of continuous and short fiber reinforced cementitious composites
l_{rf}	minimum crack spacing of multi-scale fiber reinforced cementitious composite
l_u	damage propagation length
L_f	length of the short fiber
$L(V_f)$	simplified CDF of fiber volume fraction
m	the number of bond springs between the crack springs
m_0	shape parameter of Weibull distribution of flaw size
n	the number of crack springs
n_c	the number of opening crack springs
$p(\theta)$, $p(z)$	probability density functions of the random fiber orientation and location
$p(V_f)$	probability distribution function (PDF) of fiber volume fraction
$P(V_f)$	CDF of fiber volume fraction
P_0	interface friction of a single inclined fiber
P_{pully}	frictional pulley force of a single inclined fiber
r_f, r_r	radius of the short and continuous fiber
s	slip between concrete and tensile steel bar
s_1, s_2	coefficients defining the relation between flaw size and fitting factor
s_u	slip at ultimate bond stress
s_{max}	slip at the end of bond-slip relationship
s_{fu}	slip at the beginning of the softening branch
S_r	perimeter of a single continuous fiber
u_r u_m	axial displacements of the fiber and matrix
U	random occurrence of the minimum fiber content in the opening crack springs
V_m, V_r, V_f	matrix, continuous and short fiber volume fraction
V_{f0}	short fiber design volume fraction in the mix proportion
V_{f1} $\sim V_{fnc}$	fiber volume fractions of the 1st $\sim$ n_c th crack spring
Y_f	fiber correction factor
Y_1	geometric correction factor
α	disperse coefficient
α_1, α_2	analytical coefficient for the linear bond-slip relationship
β	slip-hardening coefficient
β_1, β_2	analytical coefficient for the nonlinear bond-slip relationship
δ_{ck}, δ_{pb}	COD at cracking stress and ultimate bridging stress
δ_1, δ_2, δ_{max}	critical COD in the multiple-stage relationship
ε_{mc}, ε_{pc}	strain at the end of the multiple-cracking zone and post-cracking zone
G_f	interfacial fracture energy
G_d	chemical bond strength
ζ	monotonically increasing function
η	composite modulus coefficient
θ	angle between the loading axis and inclined fiber
λ_1	nonuniformity coefficient of crack development
λ_p	percentage error for the conversion from a normal distribution to a uniform distribution
λ_θ	angle distribution coefficient
σ_r	tensile normal stress of the continuous fiber
σ_{r0}	normal stress of the continuous fiber at the fixed end
σ_{rl}	normal stress of the continuous fiber at the loading end
σ_{rlu}	normal stress of the continuous fiber at the damage propagation length
σ_{ckf}	mean tensile strength of composite members
σ_{mc}	average ultimate strength of the composite members
σ_{mu}	cracking strength at the crack plane
σ_{ck}, σ_{pb}	composite cracking strength and ultimate bridging strength
σ_1, σ_2	critical bridging stress in the multiple-stage relationship
τ_f	short fiber-matrix bond strength
τ_r	residual bond strength
$\overline{\tau_r}$	average bond strength along the matrix-continuous fiber interface
τ_u	bond strength between continuous fiber and matrix
τ_{ue}	modified bond strength between continuous fiber and matrix
τ_{fu}	bond strength between continuous fiber and composites containing short fibers
τ_{frs}	interfacial shear stress of the continuous fiber
υ	standard deviation of normal distribution of fiber volume fraction
χ	fitting factor for cracking strength

of mix composition and tailored short fibers. The average crack width of the strain-hardening SFRC can be controlled to less than 100 μ m, making it a durable material under environmental exposures. However, the tensile performance of SFRC exhibits the limited load carrying capacity and strong variation due to the rheological behavior of the matrix [13], curing and construction conditions [14], the distribution of pores [15], fiber dispersion and agglomeration tendency [16].

The composites containing reinforcing fibers at multiple scales were proposed firstly as externally bonded composite systems for strengthening existing structures [17], and could also be applied in the construction of thin-walled structures, ocean structures [18] and permanent formworks [19], as alternatives to CFRCs or SFRCs. The mechanical behavior of the composites, including ECC-FRP [20–22], UHPC-FRP [18, 19], ECC-steel bar [23–25], UHPC-steel bar [26], etc., has been investigated experimentally. It was found that the mechanical performance was critically determined by the synergetic effect between reinforcing fibers at different scales and stochastic nature. Then, several theoretical models [27,28] and numerical approaches [29] have been proposed for the mechanical behavior of a particular kind of composites. However, a compatible and universal model, which can simulate any composite containing one or more reinforcing fibers with the consideration of stochastic nature, has not yet been developed.

In this paper, MSFRCs are proposed to systematically describe the tensile behavior of the composites. Then, the composite actions of the MSFRCs, namely, the synergetic effects on the bond performance and cracking behavior, tension stiffening and ductility enhancing effects, are discussed in terms of the bond-slip mechanism and fiber-bridging model. In addition, a 1-D numerical approach using spring elements is developed to predict the tensile response and crack description of the MSFRCs. Finally, the tensile response and crack propagation of six independent experiments obtained from literatures are simulated to verify the reliability of the developed model.

2. Mechanisms for MSFRC in tension

The matrix reinforced with fibers at multiple scales is named as the Multi-Scale Fiber Reinforced Cementitious Composite. The mechanical behavior and failure modes of the composites vary significantly with the physical properties of reinforcing fibers and the mix proportion. And, the MSFRC presents tensile characteristics of both CFRC and SFRC at the same time, but it is much more complex. Thus, the theoretical and numerical approaches for CFRCs and SFRCs will be first discussed in this section, respectively. Then, the failure modes and composite actions of MSFRCs are summarized and described based on the published experiments.

To abstract the mechanical model for 1-D uniaxial tensile behavior, seven basic assumptions are summarized: 1) fibers are only subjected to the bond force along their longitudinal axial direction, 2) bond behavior is driven by the sliding friction with a constant friction coefficient, 3) Poisson's ratio of all materials is ignored, 4) the displacements of the matrix in the same cross section have the same value, 5) all matrix cracks occur at a certain tensile stress, 6) the softening phase of cementitious matrix is ignored, and 7) reinforcing fibers behave in the elastic state during the whole loading process.

2.1. Tensile behavior and modeling of the CFRC system

How to present the effect of composite actions is the research focus of the tensile behavior of CFRC system. First, Aveston-Cooper-Kelly (ACK) theory based on the seven assumptions was proposed to establish a 1-D linear model [30], and Fig. 2(f) shows a typical tensile stress-strain response for CFRC. In the multiple-cracking stage, the stress in the continuous fibers is gradually transferred to the matrix away from the cracked plane upon crack formation. In this scenario, the minimum crack spacing can be calculated by the equilibrium condition along the loading axis for the matrix between two cracks:

$$\sigma_{mu} V_m = F_r \tag{1}$$

where $F_r = l_r \overline{\tau_r} S_r V_r / A_r$ is the interface frictional force along the continuous fiber. The minimum crack spacing of CFRC can be written as:

$$l_r = \frac{\sigma_{mu} V_m r_r}{2 V_r \overline{\tau_r}} \tag{2}$$

where $r_r = 2A_r/S_r$ is the equivalent radius of continuous fibers, and A_r and S_r are the area and perimeter of a single continuous fiber, respectively. V_m and V_r are the matrix and continuous fiber volume fraction (reinforcement ratio), respectively. $\overline{\tau_r}$ is the average bond strength along the matrix-continuous fiber interface. The cracking strength σ_{mu} at the crack plane can be taken as the average tensile strength of matrix f_{tm}.

According to assumption 5), all cracks tend to open and extend with the same crack spacing at the same time. However, since the cracking strength at different matrix planes follows a random distribution based on the weakest link theory [31], the crack always occurs in the link with the largest flaw size rather than forming uniformly. Then, for most CFRCs including steel or FRP bar reinforced concrete, the composite strains at the end of the multiple-cracking zone and post-cracking zone (i.e., ε_{mc} and ε_{pc}) can imply the tension stiffening effect, which can be calculated by the average strain of the continuous fiber according to the ACK theory [30]. Furthermore, the β-ellipse model [11] was proposed to consider the nonlinear bond-slip behavior and tension softening relationship of quasi-brittle material, instead of linear sliding friction and simplified post-cracking behavior based on assumptions 2) and 6). In addition, especially for TRC, the core and sleeve model [32] can be used to describe the unique bonding mechanism of FRP textile [33].

To consider the modifications and extend the 1-D model, advanced numerical methods are required. Depending on whether the interface and cracks are expressed as the geometrical discontinuity in the displacement field, the numerical methods for CFRC can be divided into the smeared and the discrete crack approaches. For CFRC with a sufficient reinforcement ratio, both approaches can yield mesh-independent solutions [34,35]. In addition, since the discontinuum is assumed a priori with the traction-separation law, the discrete crack approach is

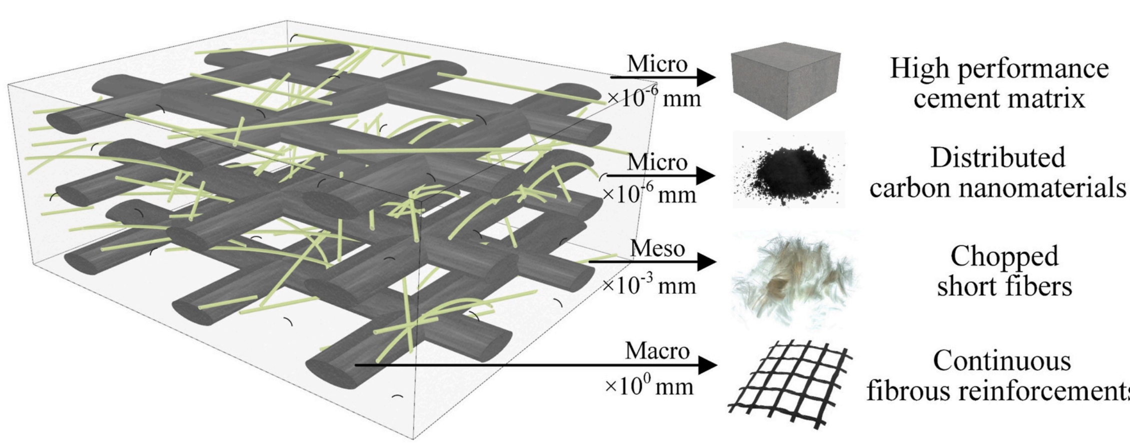

Fig. 1. Sketch of multi-scale fiber reinforced cementitious composite.

applicable to obtain the details of each crack and address the issues associated with the complicated interface [35].

2.2. Tensile behavior and modeling of the SFRC system

The micromechanics-based approach for predicting the fiber-bridging behavior of chopped short fibers and CNMs, has been extensively investigated. Tension-softening SFRC can reach a higher cracking strength and energy absorption capacity than ordinary cementitious matrix due to the fiber bridging effect, as well as the nucleation and filling effects of CNMs [36–38]. However, the bridging stress-crack opening displacement (COD) relationship proceeds into a tension softening branch after matrix cracking, resulting in the low resistance to cracking. In other words, tensile behavior of the composite is similar to that of the CFRC with insufficient reinforcements. The crack band widths of these composites can be obtained by the trial-and-error approach [39].

For strain-hardening SFRC, the snubbing coefficient f was introduced to describe the amplification of the bridging force by the frictional pulley force P_{pully}, when the inclined fiber at the angle θ with the loading axis was pulled out. Then, with assumptions 2)-7), the simplified bridging stress-COD relationship was presented by Li and Leung [6], and the minimum crack spacing l_f is given in Appendix A. Furthermore, considering the nonlinear behavior during the fiber debonding and pull-out stage, the modified crack spacing model and fiber-bridging model were developed [7] by introducing chemical bond strength G_d, slip-hardening coefficient β and fiber strength reduction f'.

According to the weakest link theory, material heterogeneities affect the crack formation of SFRC, which is similar to the cracking pattern of CFRC. To address this issue, physical properties of the composite need to be considered as the random variables, including the inherent defect of matrix and the scatter of fibers. First, the methods for quantitative evaluation were proposed to define the statistical distribution of the random variables, such as detecting the cross section sliced from the specimen [40], transmission X-ray photography [41], etc. Then, two stochastic processes were proposed to assign the random values for the stochastic model. The stochastic process based on the morphology [7] can present the correlation of random variables between adjacent elements to a certain extent. Alternatively, another stochastic process based on the statistics of extremes [42–44] becomes a desirable method, since

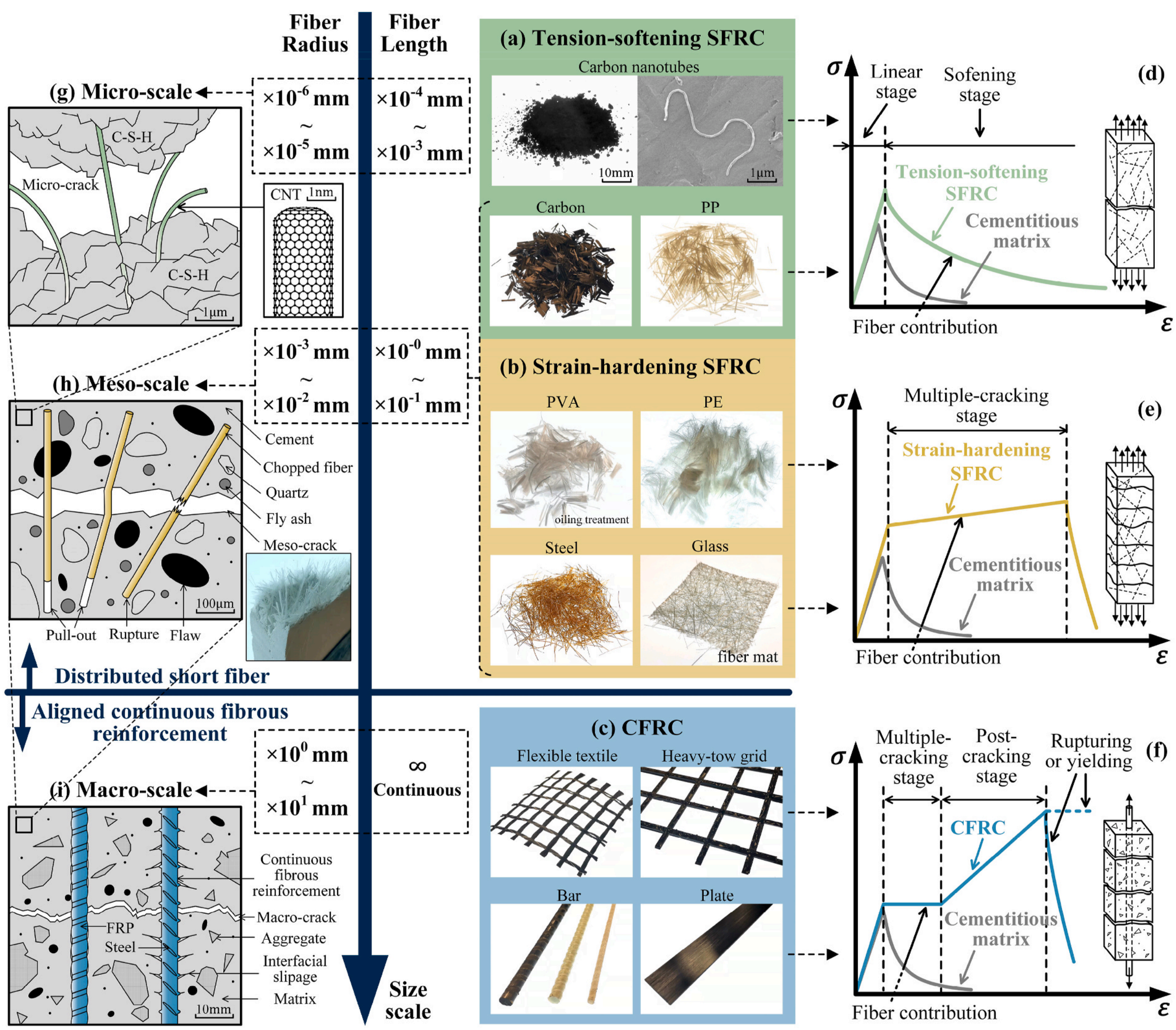

Fig. 2. Schematic of multi-scale reinforcing fibers and the tensile performance of the composites: (a)–(c) the material types and geometry properties of reinforcing fibers in SFRC and CFRC (The electron microscopy image of CNT is from Ref. [2]. Tension-softening SFRC can convert into strain-hardening SFRC by modifying the physical properties and controlling the surface roughness of reinforcing fibers [3–5]. The untailored properties of fibers, which would lead to the tension-softening SFRC, are as follows: for carbon chopped fibers, L_f = 6–12 mm, r_f = 3.4~6 μm, E_f = 48–268 GPa, σ_{fu} = 690–4600 MPa and $V_f \leq 3\%$; for PP chopped fibers, L_f = 8 mm, r_f = 8.3 μm, E_f = 3.5–11.6 GPa, σ_{fu} = 400 MPa and $V_f \leq 2\%$), (d)–(f) cracking patterns and typical tensile behavior of the CFRC, tension-softening and strain-hardening SFRC, and (g)–(i) bridging representations of reinforcing fibers under the individual scale level.

fewer random variables are acquired.

To simulate the uniaxial tensile behavior of SFRC and investigate the influence of random variables, several stochastic numerical models were developed based on the discrete crack approach, which can be divided into the fixed spacing approach and regular spacing approach. The fixed spacing approach was proposed in the literature [44,45] based on crack springs with a spacing of l_f. In this case, the random variables in different sections can be assumed to be independent, since the sequence of the cracks would not change the failure pattern. Although the distances between opening cracks are multiples of l_f, the average crack spacing still agrees quite well with the test results. For the regular spacing approach proposed in the literature [7,42,43], once the stress of the intact crack element exceeds the cracking strength, an additional examination should be conducted to ensure that the intact element is not within l_f of the existing cracks. This approach focuses on the details of each crack, and the modified crack spacing model can be applied. Based on the probability theory, the amount of the random variables under the independent and identically distributed assumption increases with the growth of mesh density, which may lead to a lower expected value of the weakest link. Thus, the stochastic process with the position-dependent probability is suggested to ensure the mesh independence for regular spacing approach.

2.3. Composite actions of the MSFRC system

Current studies on tensile response demonstrate that effective cooperation can be achieved between the reinforcing fibers at multiple scales until failure occurs in one of them. Based on the failure sequence of the reinforcing fibers, the tensile behavior of MSFRC can be divided into three modes: 1) the end of the elastic stage for continuous fibers (rupturing for FRP and yielding for steel) occurs first; 2) the softening of fiber-bridging relationship for short fibers occurs first; 3) the simultaneous failure, from tensile experiments [20,25], represents that the bridging stress of short fiber and the tensile stress of continuous fiber can reach the ultimate state at the same time, even if the SFRC exhibits a lower ultimate strain individually than that of the continuous fiber.

Since the synergetic effect between the reinforcing fibers at different scales, the composite actions of CFRCs also exist in MSFRCs but show different mechanical behavior, that is, the fiber bridging effect can bring more unique effects. Therefore, according to the fiber-bridging model and bond-slip mechanism, composite actions in MSFRCs are presented as follows:

(1) Synergetic effect on bond-slip performance

The bond behavior of continuous fibers in SFRC is quite different from that in the brittle matrix. The fiber bridging force along the circumferential direction can present the confinement effect to restrain the extension of internal cracks. Therefore, the SFRC shows the performance of withstanding larger circumferential deformation and enhancing higher sliding friction than brittle matrix. On the other hand, the axial component of the bridging force can optimize the orientation of the principal stresses and effectively arrest splitting cracks [46]. Due to the nucleation effect, the addition of CNMs also can improve the bond between other reinforcing fibers and matrix [47,48].

(2) Synergetic effect on cracking behavior

The short and continuous fibers at the crack planes become engaged after matrix cracking. In other words, the discontinuous crack opening will activate the interfacial friction of the matrix-reinforcing fibers, and the tiny pulled slip of short fibers at the crack is compatible with the deformation of the continuous fiber. Thus, the combination of the reinforcing fibers can participate in the transferring force between cracks, which has a great influence on the crack spacing [27,28]. In this paper, the theoretical formula of the minimum cracking spacing will be discussed in the next section. On the other hand, the tension-softening behavior of matrix for CFRC should be replaced by fiber-bridging behavior as the traction-separation law. In this situation, the mesh convergence for the discrete crack approach need to be studied.

(3) Tension stiffening effect in the multiple-cracking stage

For MSFRC, the external force can be greater than that of either composite and it keeps increasing with the formation of multiple fine cracks due to the strain compatibility. In terms of the bond mechanism, the improvement of bond strength and the decrease of the crack spacing have the opposite effect on the stress distribution along the continuous fiber. In previous studies, it was found that the ε_{mc} obtained from experimental results was close to the strain of continuous fibers at the end of the elastic stage [24,25]. In contrast, several results indicated the opposite phenomenon in which the nonuniformity along the rebar was greatly increased [23,26], possibly due to the matrix shrinkage. Therefore, the extent to which the experimental results conducted thus far are suitable remains problematic for theoretical analysis purposes.

(4) Tension stiffening effect in the post-yielding stage (crack localization)

For RC tensile members, the residual bond between the continuous fiber and matrix can lead to the early rupture of the steel bar in post-yielding stage, as shown in Fig. 3(a). Since large deformations are not allowed in structural design, there are few studies on the rupture strain of steel bar in RC members. However, compared with RC members, an early fracture mode of MSFRC, characterized by sudden failure and crack localization in one or a few dominantly wide cracks, has been observed in recently reported experiments [24,26], and the crack localization will lead to a much lower ultimate strain. As explained in Fig. 3(b), the minute crack opening displacement provides the precondition for the concentrated crack pattern, and the crack localization phenomenon is related to the V_r, V_f and short fiber dispersion [49]. As a result, the crack localization should be avoided in any structural member to preserve its deformation capability.

(5) Ductility enhancing effect

For the MSFRC members characterized by the simultaneous failure mode, the pseudo-ductility of SFRC under the reinforcement of the continuous fibers can be enhanced, and the phenomenon is referred to as the ductility enhancing effect in this paper. Fig. 4 presents the mechanism of the ductility enhancing effect based on the probabilistic analysis. During the whole loading process, the 2nd crack remains intact since $\sigma_{ck,2} > \sigma_{pb,1}$, as shown in Fig. 4(a). However, when the SFRC is reinforced with continuous fibers, the stress of the 2nd crack can be increased due to the bond contribution, which would lead to matrix cracking in the 2nd crack. Then, the extension of crack widths in the 1st and 2nd cracks contribute to a higher pseudo-ductility at the composite level. In conclusion, the analysis of the ductility enhancing effect requires a probabilistic approach based on the statistical distribution, as well as the crack localization phenomenon.

3. Modeling for MSFRC in tension

A stochastic numerical approach is created to simulate the tensile behavior for MSFRC. To simplify the uniaxial specimen as multiple parallel elements, the basic assumptions 3) and 4) are applied. In addition, the stochastic process based on the statistics of extremes and the fixed spacing approach proposed in the literature [44,45] are used, in other words, the length of each uncracked matrix element is the minimum crack spacing l_{rf}.

Fig. 5 shows the basic truss-spring system of the 1-D numerical

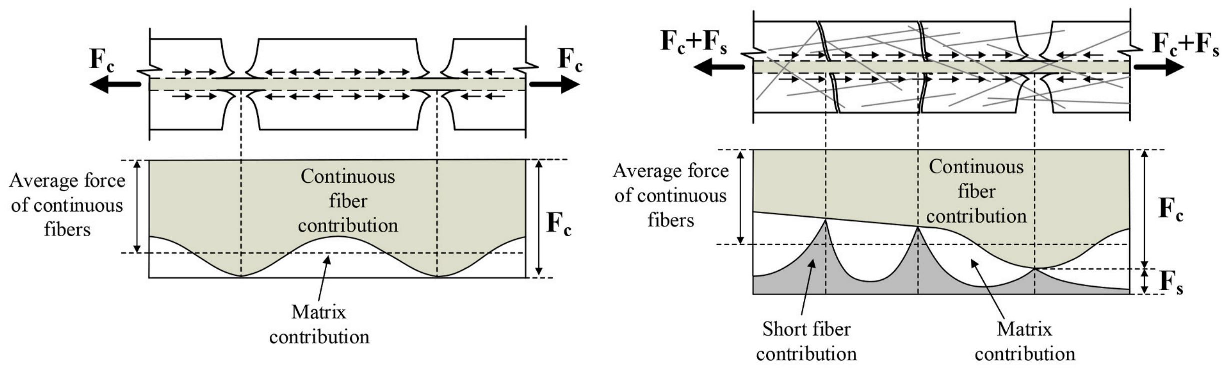

(a) Force contribution of CFRC (b) Force contribution of MSFRC

Fig. 3. Difference in the crack pattern between CFRC and MSFRC at the ultimate limit state.

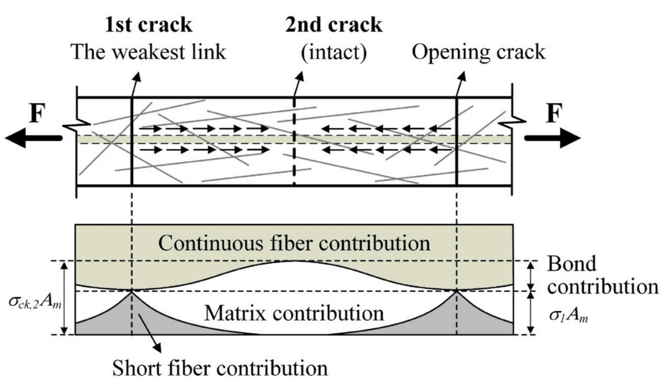

(a) Force contribution before the opening of 2nd crack

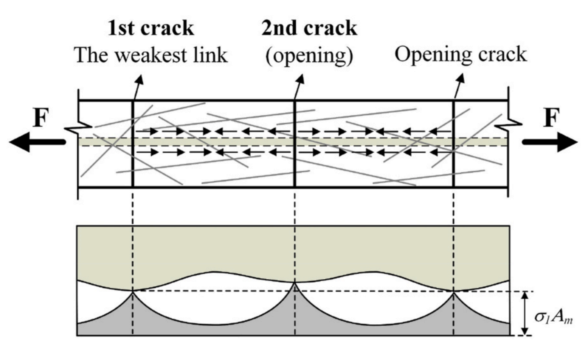

(b) Force contribution after the opening of 2nd crack

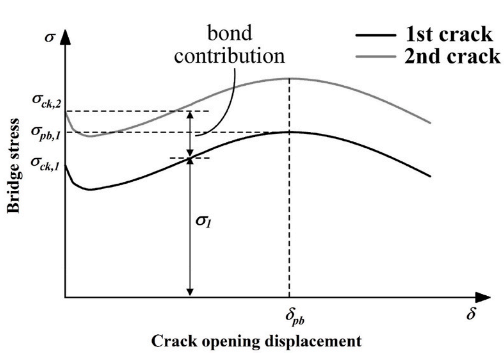

(c) The stress-COD relationships of 1st crack and 2nd crack

Fig. 4. The mechanism of the ductility enhancing effect.

model. The uncracked matrix and continuous fiber are both simulated as the continuum truss elements. Several sets of shear spring elements, describing the bond performance, are applied to connect the matrix elements with the continuous fiber elements. The relationship of bond elements reflects the tension stiffening effect. In addition, there are tensile spring elements between matrix continuum elements, where the tension softening effect of the matrix and the fiber-bridging mechanism can be expressed. Two types of random variables are applied to represent the stochastic nature, and Monte Carlo simulation is performed to determine the effect of the stochastic nature on the composite tensile behavior.

As discussed above, two kinds of springs are used to capture the details of the crack width and modify the constitutive law with respect to various fiber types and material randomness. In this way, the developed model deteriorates into the CFRC model when the crack spring elements are described by the tension softening relationship of concrete, and into the SFRC model when $V_r = 0$. Hence, it is necessary to obtain the constitutive laws for each element and the minimum crack spacing.

3.1. Stress-COD relationship for crack spring element

As illustrated in Fig. 6, the multiple-stage stress-COD relationship is applied on the basis of the research [44]. The stress fluctuation caused by the sudden energy release of matrix cracking is replaced by the constant stress phase to reduce the iterations in the convergence process. When the mechanical properties of short fibers have been acquired by the high-accuracy experiments for a single fiber, the relationship can be determined by appropriate theoretical model: β-ellipse model for concrete [11], fiber-bridging model for SFRC containing chopped short fibers [6,7]. In the absence of the mechanical properties, direct test methods can be conducted to determine the relationship [50].

3.2. Random variables for crack spring element

To present the ductility enhancing effect and the crack localization, the matrix flaw size c and fiber volume fraction V_f are simulated as the independent and identically distributed random variables. Then, n couples of (c, V_f) are generated and are assigned to each crack spring by stochastic processes. Therefore, the distribution functions and the relationships associated with the variables and fiber-bridging law need to be identified.

3.2.1. Matrix flaw size and cracking strength

Based on the weakest link theory, the matrix flaw size is assumed to follow the Weibull distribution, and the cumulative distribution function (CDF) can be described as follows:

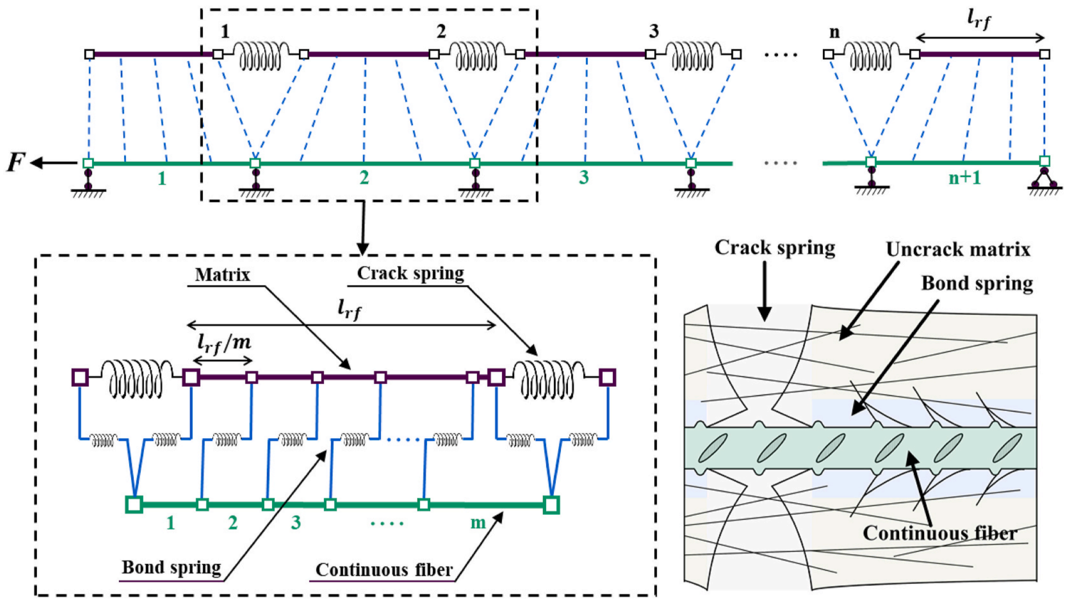

Fig. 5. Details of the proposed numerical model.

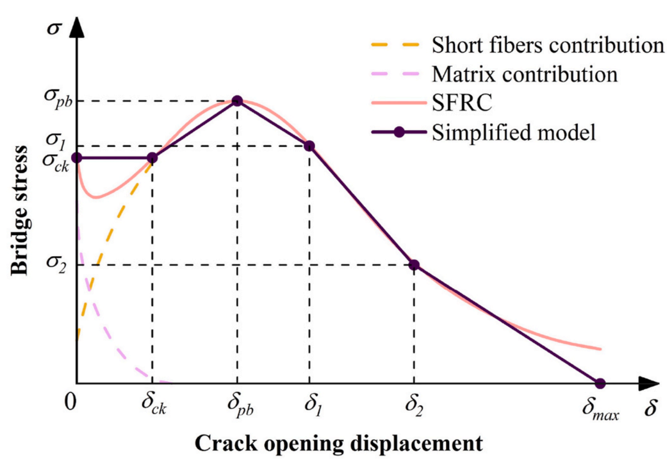

Fig. 6. Simplified constitutive law for crack spring element in tension.

$$F(c) = 1 - \left\{ exp\left[- \left(\frac{c}{c_0} \right)^{m_0} \right] \right\}^{\frac{L}{L_0}} \tag{3}$$

where c_0 and m_0 are the scale parameter and shape parameter, calibrated by fitting the statistical data. The power law scaling defined as the element length L to the reference length L_0, could be considered as 1 based on the independent and identically distributed assumption.

According to linear elastic fracture mechanics (LEFM), the formulation about the cracking strength σ_{ck}, matrix fracture toughness K_m, c and fiber mechanical properties can be established. For the brittle matrix, σ_{ck} can be written as:

$$\sigma_{ck} = \frac{K_m}{\sqrt{Y_1 c}} \tag{4}$$

where Y_1 is the geometric correction factor. Specifically, $Y_1 = \pi$ for the central straight crack and $Y_1 = 2/\pi$ for the penny shaped crack. For SFRC, the contribution of fiber bridging should be added to the crack as cohesive traction, and σ_{ck} of SFRC given by Li [6] is rewritten as:

$$\sigma_{ck} = \frac{K_f}{\sqrt{Y_1 Y_f c}} \tag{5}$$

where $K_f = (1+\eta)K_m$ corresponds to the fracture toughness with consideration of the short fiber contribution. Moreover, Y_f, the fiber correction factor considering the fiber bridging effect, is rewritten as:

$$Y_f = \frac{1}{1 - Y_2 c + Y_3 c^{\frac{3}{4}}} \tag{6}$$

$$Y_2 = \frac{Y_1 \sigma_{pb}\left(1 - v^2\right)}{\pi \delta_{pb} \eta V_m E_m} \tag{7}$$

$$Y_3 = \frac{4}{3}\sqrt{\frac{Y_1 Y_2 \sigma_{pb}}{K_f}} \tag{8}$$

Hence, Eq. (5) becomes (4) when $V_f = 0$. Nevertheless, for a small initial crack, the theoretical formulation based on LEFM tends to overestimate the cracking strength due to the fracture process zone [51]. Thus, Y_f in Eq. (5) can be replaced by the fitting factor χ in a similar form based on the research by Huang and Zhang [44]:

$$\chi = \frac{1}{c/s_1 + 1/s_2} + 1 \tag{9}$$

where s_1 and s_2 are the coefficients to consider the fracture process zone and reinforcing mechanism of fibers at micro- and mesoscopic scales. To calibrate the parameters, three sets of (c, σ_{ck}) determined from experimental data, are provided by the following: (c_{ckm}, f_{tm}) the mean tensile strength of the matrix obtained by material standard tests and the largest radius of the flaws in failure sections; (c_{ckf}, σ_{ckf}) the mean cracking strength of composite members and the largest radius of the flaws in the first cracking sections; and (c_{mc}, σ_{mc}) the average ultimate strength of the composite members and the largest radius of the flaws in failure sections. c_{mc} also represents the critical flaw size, which can be evaluated by combining Eq. (5) and $\sigma_{ck} = \sigma_{mc}$ [45].

The flaw sizes c_{ckm} and c_{ckf} of CFRC specimens in the failure sections are generally not measured. In this case, s_1 and s_2 can be deduced by using the definition of the mean tensile strength f_{tm} and characteristic tensile strength f_{tk}:

$$E(\sigma_{ck}(c, s_1, s_2)) = f_{tm} \tag{10}$$

$$P_r\left(c < c_{ckf}\right) = 0.95 \tag{11}$$

Eqs. (10) and (11) imply that the average cracking strength is equal to f_{tm}, and only less than 5% of the crack springs would fail as the stress is less than f_{tk}. In addition, f_{tk} can be expressed by f_{tm} according to the Chinese concrete design code [52]: $f_{tk} = f_{tm}k(1 - 1.645\alpha)$; k and α are the brittle and disperse coefficients, respectively.

3.2.2. Fiber volume fraction and ultimate bridging stress

The fiber volume fraction of each crack spring element can be regarded as an inherent property. Assuming that V_f follows a normal distribution, $p(V_f)$ can be given by:

$$p\left(V_f\right) = \frac{1}{\sqrt{2\pi v^2}}\exp\left[-\frac{\left(V_f - V_{f0}\right)^2}{2v^2}\right] \tag{12}$$

In this distribution, V_{f0} stands for the expected value, which is equal to the design volume fraction of short fibers in the mix proportion; v, the standard deviation of the distribution, can be obtained by fitting the statistical distribution from the sampling measurements. The ultimate strength in the particular section can be obtained by assuming that σ_{pb} is proportional to the fiber content V_f via [50]. However, since few experiments have captured fiber dispersion data, a fitting method is proposed to estimate $p(V_f)$. The v can be obtained via the expectation of the random occurrence $U = min(V_{f1}, V_{f2}, \dots, V_{fnc})$:

$$E(U) = \frac{\sigma_{mc}}{\sigma_{pb}}V_{f0} \tag{13}$$

where n_c is the number of opening crack springs. $V_{f1} \sim V_{fnc}$ are the fiber volume fractions of the 1st$\sim$ n_c th crack spring. Once the flaw size distribution and c_{mc} are identified, n_c can be predicted in terms of the number of all crack springs n by the following:

$$n_c = (1 - F(c_{mc}))n \tag{14}$$

The derivation of l_{rf} is given in Section 3.4. However, it is a concern that n_c cannot be calculated when the flaw size distribution and c_{mc} have not been determined statistically. In this scenario, n_c is given in terms of the average peak strain measured by the test ε_{pb} as follows:

$$n_c = \frac{\varepsilon_{pb}l_{rf}(n+1)}{\lambda_1\delta_{pb}} \tag{15}$$

where λ_1 empirically describes the nonuniformity of crack development, and $\lambda_1 = 0.8$. Then, in terms of the CDF $P(V_f)$, the expectation of U is derived as:

$$E(U) = \int_{-\infty}^{\infty} n_c V_f\left(1 - P\left(V_f\right)\right)^{n_c - 1} p\left(V_f\right) dV_f \tag{16}$$

Based on the above analysis, v can be solved by substituting Eq. (16) into (13). To simplify the calculation process, the linear CDF $L(V_f)$, i.e., the uniform distribution defined in $[V_{fm}, 2V_{f0} - V_{fm}]$, is implemented to approximate $P(V_f)$. Then, Eq. (16) can be rewritten as:

$$E(U) = V_{fm} + \frac{2\left(V_{f0} - V_{fm}\right)}{n_c + 1} = L^{-1}\left(\frac{1}{n_c + 1}\right) \tag{17}$$

An accurate approximation of the normal distribution integral was provided by the error function defined as $erf(V_f) = (2/\sqrt{\pi})\int_0^{V_f} exp(-t^2)dt$. By substituting $P(V_f) = \lambda_p L(V_f)$ into Eq. (17), v can be determined by the following:

$$v = \frac{\left(\frac{\sigma_{mc}}{\sigma_{pb}} - 1\right)V_{f0}}{\sqrt{2}erf^{-1}\left(\frac{2\lambda_p}{n_c + 1} - 1\right)} \tag{18}$$

where λ_p represents the percentage error for the conversion from a normal distribution to a uniform distribution, and $\lambda_p = 1$ approximately based on the simulated results.

3.3. Constitutive relationship for the truss elements

The constitutive relationship of the uncracked matrix can be described by the linear elasticity. For steel or FRP rebar, the stress-strain constitutive relationship can be applied by the response from the material tensile tests. In the absence of the complete measured curve, a monotonic stress-strain model with four parameters for steel [53] and linear relationship for FRP can be implemented for the truss elements. For FRP textile, the core and sleeve model can be adopted to describe the unique phenomena, such as nonuniform stress distribution and initial slack [32]. However, the details of the initial waviness and the filament-filament bond mechanism have not been investigated thoroughly, simulations for composites containing FRP textiles will be carried out in future research.

3.4. Local bond-slip relationship for the bond spring element

Bond-slip constitutive relationships for CFRC and MSFRC described in Fig. 7 are applied according to the synergetic effect on the bond performance. The simplified bond-slip model of CFRC with the linear softening branch proposed by Haskett [54] is applied in this paper:

$$\tau = \begin{cases} \tau_u\left(\dfrac{s}{s_u}\right)^{0.4} & (s \le s_u) & \text{(19a)} \\ \tau_u\dfrac{s_{max} - s}{s_{max} - s_u} & (s_u < s \le s_{max}) & \text{(19b)} \end{cases}$$

where τ_u, s_u, s_{max} and G_f are defined in Fig. 7. The bond strength can be given by $\tau_u = 2.5\sqrt{f_c}$. The parameter s_u is suggested by Lin [55] as follows:

$$s_u = 0.12C_{clear}\zeta(K) \tag{20}$$

$$\zeta(K) = \frac{1}{1 + ae^{bK}} \tag{21}$$

where C_{clear} is the clear distance between lugs. The confinement parameter $K = c_m/2r_r$ for plain concrete, represent the confinement effect by matrix cover c_m. The empirical parameters a and b can be determined through regression analysis based on the test results. Interestingly, according to the improved pull-out tests in the literatures [56], the value of s_u is approximately 0.05 mm, far lower than the results of the traditional pull-out test of 0.3$\sim$2 mm. This difference is attributable

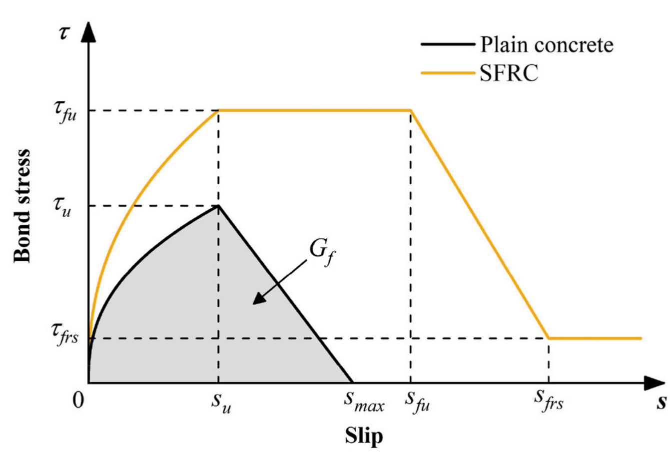

Fig. 7. Local bond-slip constitutive laws for bond spring element.

to the comprehensive stress state of the rebar-matrix interface. The improved pull-out test are pulled from both sides of the continuous fiber, and the matrix stress state is close to that of the uniaxial tension test [57]. Thus, the results of the improved pull-out tests are adopted to calibrate a and b for s_u. The parameter s_{max}, which governs the descending branch of the bond-ship constitutive relationship, presents high scatter for determining the precise value due to the brittle interfacial behavior [58]. Thus, the difference between s_{max} and s_u is regarded as a constant value in this research and determined from the test results.

For MSFRC, the bond-slip constitutive model proposed by Harajli [59] is applied with respect to the synergetic effect on the bond mechanism. The relationship of MSFRC can be determined expediently from the relationship of RC in terms of the bridging parameter c_f as follows:

$$\tau_{fu} = c_f \tau_u \tag{22}$$

where $c_f = 1 + 0.34\sqrt{V_f L_f / 2r_f - 0.25}$ for $V_f L_f / 2r_f \geq 0.25$ and $c_f = 1$ for $V_f L_f / 2r_f \leq 0.25$. $s_{fu} = 2.33 s_u$ implies the improvement of the ultimate interfacial ductility. The residual bond strength τ_{frs} can be taken according to the experimental results.

3.5. Minimum crack spacing for matrix element length

Since the stress transferred by interaction within the minimum crack spacing l_{rf} cannot reach the matrix strength, l_{rf} is utilized as the length between the crack spring elements. The interfacial forces of both continuous and short fibers are transferred to the matrix through F_r, F_f and F_{pulley}, and the equilibrium condition of the matrix plane can be derived:

$$F_f + F_{pulley} + F_r = \sigma_{mu} V_m \tag{23}$$

The released stress of the matrix cracking is completely carried by short fibers and continuous fibers in the cracking plane, and the inner force for a single fiber P_0 can be acquired by:

$$P_0 = \frac{(\sigma_{mu} V_m - F_r)}{g V_r} \pi r^2 \tag{24}$$

Then, the resultant pulley force for MSFRC can be rewritten as:

$$F_{pulley} = (\sigma_{mu} V_m - F_r)\left(1 - \frac{1}{\lambda_\theta g}\right) \tag{25}$$

Substituting F_{pulley}, $F_{friction}$ and F_r into Eq. (24), the minimum crack spacing l_{rf} for MSFRC can be derived as:

$$l_{rf} = \frac{\left(1 + \frac{l_f'}{l_r'}\right) L_f - \sqrt{\left(\left(1 + \frac{l_f'}{l_r'}\right) L_f\right)^2 - 4 L_f l_f'}}{2} \tag{26}$$

where $l_f' = \sigma_{mu} V_m r_f / (g V_f \tau_f)$ and $l_r' = \sigma_{mu} V_m r_r / (2 V_r \overline{\tau_r})$ are defined as the transmission lengths of the short and continuous fibers, respectively. $\overline{\tau_r}$ is the average bonding strength along the matrix-continuous fiber interface, which can be obtained from the global bond-slip response. Since the local bond-slip relationship is utilized in this numerical method, it is necessary to provide a connection between the global and local response. The bond mechanism and details for calculating $\overline{\tau_r}$ by the pull-out model are described in Appendix B. Then, l_{rf} can be determined by combining $\overline{\tau_r}$ and Eq. (26).

If Eq.(26) have a real positive root, $l_{rf} < l_f$ and $l_{rf} < l_r$ hold, indicating that average crack spacing of MSFRC can be constrained effectively with a range of about 2–10 mm [22,23]. In the absence of a real root, l_{rf} deteriorates into l_r due to the limited enhancement of short fibers, and the average spacing of CFRC is generally around 100 mm [28,60]. Since the crack spacing of CFRC are at least one order of magnitude higher than that of MSFRC, the critical $\overline{\tau_r}$ can be approximated by the extreme value at $l_{rf} \to 0$:

$$\overline{\tau_r} = \frac{r_r}{2 l_{rf}} \left[\frac{\sigma_{rlu} \cos(\beta_1 l_{rf}) + \frac{2\tau_u}{\beta_1 r_r} \sin(\beta_1 l_{rf})}{1 - \frac{\beta_2}{\beta_1^2} + \frac{\beta_2}{\beta_1^2} \cos(\beta_1 l_{rf})} - \sigma_{rlu} \right] \tag{27}$$

It is found that $\overline{\tau_r}$ approaches τ_u as $l_{rf} \to 0$. As explained above, when the strain-hardening conditions are satisfied by fiber and interface tailoring, $\overline{\tau_r}$ can be simplified to τ_u. Then, l_{rf} can be easily determined.

4. Model validation for MSFRC in tension

Six independent tensile experiments are simulated based on ABAQUS to assess the accuracy of the proposed approach. For each simulated example, all of the input model parameters can be determined by the calibration method as described in Section 3. A summary of the input data is shown in Tables 2 and 3. The analyses with ten repeated stochastic models for each specimen are conducted in the Monte Carlo simulation.

First, three kinds of SFRCs are studied in the simulations, while the physical factors of different fibers and the stochastic parameters are calibrated. Next, a series of direct tensile RC members are simulated to match the mechanical response and crack evolution process with the experimental results. Finally, on the basis of the above models of CFRC and SFRC, two forms of MSFRC, namely, UHPC-steel rebar and ECC-FRP grid, are modeled and examined in terms of the composite actions.

4.1. Simulation and verification for PVA-ECC, UHPC and PE-ECC

When the matrix is only toughed by short fibers, the proposed model changes to the fixed spacing approach developed. First, for ECC specimens, most physical parameters and matrix flaw size distributions have been previously measured in the experiments reported by Wang [40] as listed in Table 3. Then s_1 and s_2 can be calibrated by substituting (c_{ckf}, σ_{ckf}) and (c_{mc}, σ_{mc}) into Eq. (5) and (9). Specifically, $c_0 = 0.97$, $m_0 = 2.12$, s_1 and s_2 are applied to all of the members containing the short fibers due to the lack of the calibrated distribution for most experiments. The fiber content distribution can be determined by the experimental results, and the fracture toughness of the matrix can be obtained via the experiments [61]. With respect to the different mix proportions used in Zheng [20], the bridging law is determined through the interface parameters with a lower fictional coefficient provided via [62], as shown in Table 1.

Second, UHPC specimens with straight and hooked steel fibers, utilized by Wang [63] and Hung [26] respectively, are modeled. The straight steel fiber, characterized by high strength and low aspect ratio, tends to be pulled out; thus, the simplified bridging relationship can be implemented without the consideration of fiber rupture. On the other hand, for UHPC with hooked steel fibers, the bridging peak stress of hooked fibers is much lower than that of straight fibers due to fiber congestion and high failure brittleness in the inclined plane [64]. However, few studies have focused on the bridging law with respect to

Table 1
Material parameters for short fibers.

Parameters	Steel-1	Steel-2	PVA-1	PVA-2
Fiber Young's modulus E_f (GPa)	200	200	25.8	25.8
Fiber length L_f (mm)	13	30	12	12
Fiber radius r_f (μm)	100	100	19.5	19.5
Fiber tensile strength σ_{fu} (MPa)	2500	2500	900	900
Frictional bond strength τ_f (MPa)	11	11	2.53	1.11
Chemical bond strength G_f (N/m)	–	–	1.49	6
Slip hardening coefficient β	–	–	0.52	0.05
Snubbing coefficient f	0.5	0.5	0.2	0.2
Strength reduction coefficient f'	–	–	0.3	0.3

Table 2
Critical points for the simplified bridging laws.

Sources	Composites	σ_{pb} (MPa)	σ_1 (MPa)	σ_2 (MPa)	δ_{ck} (mm)	δ_{pb} (mm)	δ_1 (mm)	δ_2 (mm)	δ_{max} (mm)
Wang	ECC	5.86	4.98	2.93	0.0284	0.071	0.13	0.25	1.4
Wang and Guo	UHPC, $V_f = 1.5$	8.06	6.85	4.03	0.0175	0.044	0.51	1.80	6.5
	UHPC, $V_f = 2$	10.74	9.13	5.37	0.0171	0.043	0.51	1.80	6.5
	UHPC, $V_f = 2.5$	13.43	11.42	6.72	0.0168	0.042	0.51	1.80	6.5
Yu et al.	UHTCC	17.86	15.18	3.57	0.0520	0.130	0.16	0.26	1.3
Lee and Kim	NSC	–	0.63	0.21	–	0	0.08	0.16	0.19
	HSC	–	0.67	0.05	–	0	0.08	0.16	0.26
Hung et al.	UHPC	10.24	8.70	5.12	0.0608	0.152	1.17	3.12	15
	RC-rebar	–	0.72	0.05	–	0	0.08	0.16	0.2
	UHPC-rebar	8.93	7.59	4.47	0.0608	0.152	1.17	3.12	15
Zheng et al.	ECC	3.82	3.25	1.91	0.0581	0.083	0.16	0.30	2
	ECC-FRP	3.82	3.25	1.91	0.0581	0.083	0.16	0.30	2

inclined anchorage and low fiber dispersion. Therefore, according to the experimental results by Yoo et al. [64], the σ_{pb} of specimens with hooked fibers can be approximately determined by reducing the bridging strength of the straight fibers. In addition, it is assumed that the specimens with different fiber volume contents have the same fiber dispersion, and the calibration method for υ proposed in this paper is used through the specimen with a 2.5% fiber volumetric ratio. Moreover, other physical properties of the steel fiber are determined according to previous research [65,66].

Third, PE-ECC specimens combining high mechanical strength and excellent strain-hardening behavior, are simulated according to the test results of Yu [67]. In the absence of the physical properties of PE fibers, the test data from the direct test method are used as the model parameters. Then all input factors can be determined with the assumption of uniformly dispersed fibers.

The computed stress-strain relationships of the three kinds of SFRC specimens are presented in Fig. 8. Through a comparison to the curves recorded in the experiments, it is found that the results with the proper input factors demonstrate satisfactory agreement with the experimental results. For the PVA-ECC specimens, the numerical approach can provide the tensile performance of the ECC specimens with different fiber properties, and the corresponding input factors are used in the ECC-FRP grid simulations in Section 4.4. For the UHPC, the simulation results represent that the UHPC specimens can be altered from tension-softening to strain-hardening behavior with the increase of the fiber volume fraction. Nevertheless, since the same s_1 and s_2 are employed for the specimens with different fiber contents, the contribution of steel fibers to the first cracking strength cannot be presented through the simulations. Fig. 8(h) compares the crack evolution of the weakest link in one of the simulations to that of the experiments. It is shown that the crack width of UHPC can be controlled below 0.05 mm until a localized crack occurs. In addition, the validated physical properties of the UHPC specimen with hooked fibers are applied to the UHPC-rebar simulations in Section 4.3.

4.2. Simulation and verification for RC

A series of direct tensile RC samples conducted by Lee and Kim [60] are chosen to verify the feasibility of the tensile specimens without short fibers. Six specimens differ in terms of the matrix cover thickness ($c/d = 1, 2, 3$) and the compressive strength of the concrete matrix (high-strength concrete, HSC or normal-strength concrete, NSC), which represent the different bond-slip relationships and the fracture toughness of matrix, respectively. On the basis of the flaw size distribution in the previous section, c_{ckm} and c_{ckf} are determined to be 1.628 mm and 0.63 mm by Eqs.(10) and (11), respectively. Then, (c_{ckm}, f_{tm}) and $(c_{ckf}, (1+\eta)f_{tk})$ are used to calibrate the s_1 and s_2. The empirical parameters for bond-slip relationships a, b, and s_{max} are determined based on test results in the literatures [56]. More details are provided in Fig. 9 and Tables 2 and 3.

To prove the theoretical formula of $\overline{\tau_r}$ derived from the bonding mechanism, RC models with the length of one minimum crack spacing are conducted first. As shown in Fig. 10, the slight distinction between the numerical and theoretical results is attributed to the linear simplification of the local bond-slip law. Based on the availability of the bond spring elements, Fig. 11 shows a comparison of the tensile load-average strain responses simulated by the numerical model and obtained from the tests. The average crack spacing at the multiple-cracking stage can be calculated by dividing the member length by the number of uncracked segments, as shown in Fig. 12. The good agreement between the results of the simulations and tests demonstrates that the developed approach can exhibit the composite actions.

4.3. Simulation and verification for UHPC-rebar

Three groups of composite specimens containing steel rebars and steel short fibers tested by Hung [26] are analyzed. The variables of the specimens include the size of the rebar ($d = 16, 19, 22\,mm$) and the volumetric ratio of the steel fibers ($V_f = 0, 2\%$), while the difference in loading patterns (monotonic or cyclic) is not considered. The material properties obtained from the rebar tension tests are adopted as the constitutive laws of the truss elements.

Through the initial load-strain curves shown in Fig. 13, it is found that the addition of steel fiber can increase the ultimate tensile load. The fluctuations caused by the crack formation in the response of the UHPC-rebar will not lead to sharp decreases in the tensile force due to the tiny pulled slip of short fibers. Fig. 14 shows the complete load-strain responses for the UHPC-rebar and RC specimens. Note that the force fluctuations in the RC numerical results are caused by the failure of the bond springs, and the external force can revert back to the previous peak level through the stress redistribution. Meanwhile, although the experimental results show the considerable scatter due to material randomness, the envelope of the simulation results can basically cover the test curves. In regard to the composite actions, the extent of crack localization and ductility enhancing effect shows a strong correlation to the short fiber scatter and volumetric ratios of the reinforcing fibers, which still needs further research to understand the interplay.

4.4. Simulation and verification for ECC-FRP

As per Zheng [20], uniaxial tensile samples with 2% PVA fibers and BFRP grids with different volumetric ratios ($V_r = 0.17\%, 0.68\%, 1.16\%$) are used. It is assumed that two ends of the matrix and continuous fibers can be fixed tightly. In addition, the ultimate strain of the BFRP grids of the input model is determined by the strain gauge measurements of the specimens with $V_r = 1.16\%$. The loading applied to the specimen ends, is divided by the cross-sectional area to obtain the equivalent stress, as shown in Fig. 15. In contrast to the UHPC-rebar results that the tensile responses may proceed into the softening branch after the steel rebar yields, the PVA fibers and FRP grids show good compatibility up to the

Table 3
Input parameters of all specimens for model validation.

Sources	Composites	Continuous fiber					Short fiber			Matrix		Geometry and parameters for calibration						Stochastic parameters		
		V_r	E_r	f_r	A_r	S_r	Fiber type	V_f	Fiber direction	E_m	K_m	Loading condition	l_{rf}	σ_{mu}	m	n	n_c	s_1	s_2	v
		%	GPa	MPa	mm^2	mm		%		GPa	MPa·m$^{1/2}$		mm	MPa						$\times 10^{-3}$
Wang	ECC	0	–	–	–	–	PVA-1	2	2-D	20	1.19	M	1.82	4.84	–	98	57	31.9	45.6	1.6
Wang and Guo	UHPC	0	–	–	–	–	Steel-1	1.5	3-D	48	2.58	M	5.7	–	–	34	–	31.9	45.6	1.3
	UHPC							2					5.58	–	–	35	–			
	UHPC							2.5					5.47	12.2	–	36	28			
Yu et al.	UHTCC	0	–	–	–	–	PE	2	2-D	20	2.83	M	1.6	–	20	50	–	31.9	45.6	0
Lee and Kim	NSC, $c_m/d = 1$	1.22	200	430	59.7	283.5	–	0	–	28	1.25	C	120	–	20	12	–	270.8	186.8	0
	NSC, $c_m/d = 2$												115	–		12	–			
	NSC, $c_m/d = 3$												109	–		13	–			
	HSC, $c_m/d = 1$	1.22	200	430	59.7	283.5	–	0	–	28	1.8	C	104	–	20	13	–			
	HSC, $c_m/d = 2$												92	–		15	–			
	HSC, $c_m/d = 3$												88	–		16	–			
Hung et al.	UHPC	0	–	–	–	–	Steel-2	2	2-D	48	1.51	M	12.8	6.7	–	12	6.5	31.9	45.6	5.2
	RC-rebar16	0.89	200	430	201	50	–	0	–			C + M	92	–	20	3	–	270.8	186.8	0
	RC-rebar19	1.26		445	284	60							85	–		4	–			
	RC-rebar22	1.69		469	380	69							67	–		6	–			
	UHPC-rebar16	0.89		430	201	50	Steel-2	2	3-D				10.3	–	5	28	–	31.9	45.6	5.2
	UHPC-rebar19	1.26		445	284	60							10	–		29	–			
	UHPC-rebar22	1.69		469	380	69							9.6	–		30	–			
Zheng et al.	ECC	0	–	–	–	–	PVA-2	2	2-D	20	0.72	C + M	4.68	2.8	–	31	23	31.9	45.6	2.6
	ECC-FRP1	0.17	24.4	416	3.45	8.9							3.7	–	5	40	–			
	ECC-FRP3	0.68			10.35	12.8							3.2	–	5	46	–			
	ECC-FRP5	1.16			17.25	18							2.9	–	5	51	–			

Notes: f_r is the yield strength of steel or the ultimate strength of FRP. Fiber angle can be assumed as 2-D or 3-D uniform distribution according to the thickness of the specimen and the fiber length. C and M under loading conditions imply that the displacement load is applied to the continuous fiber element or the matrix element. m is the number of the bond springs between the crack spring elements.

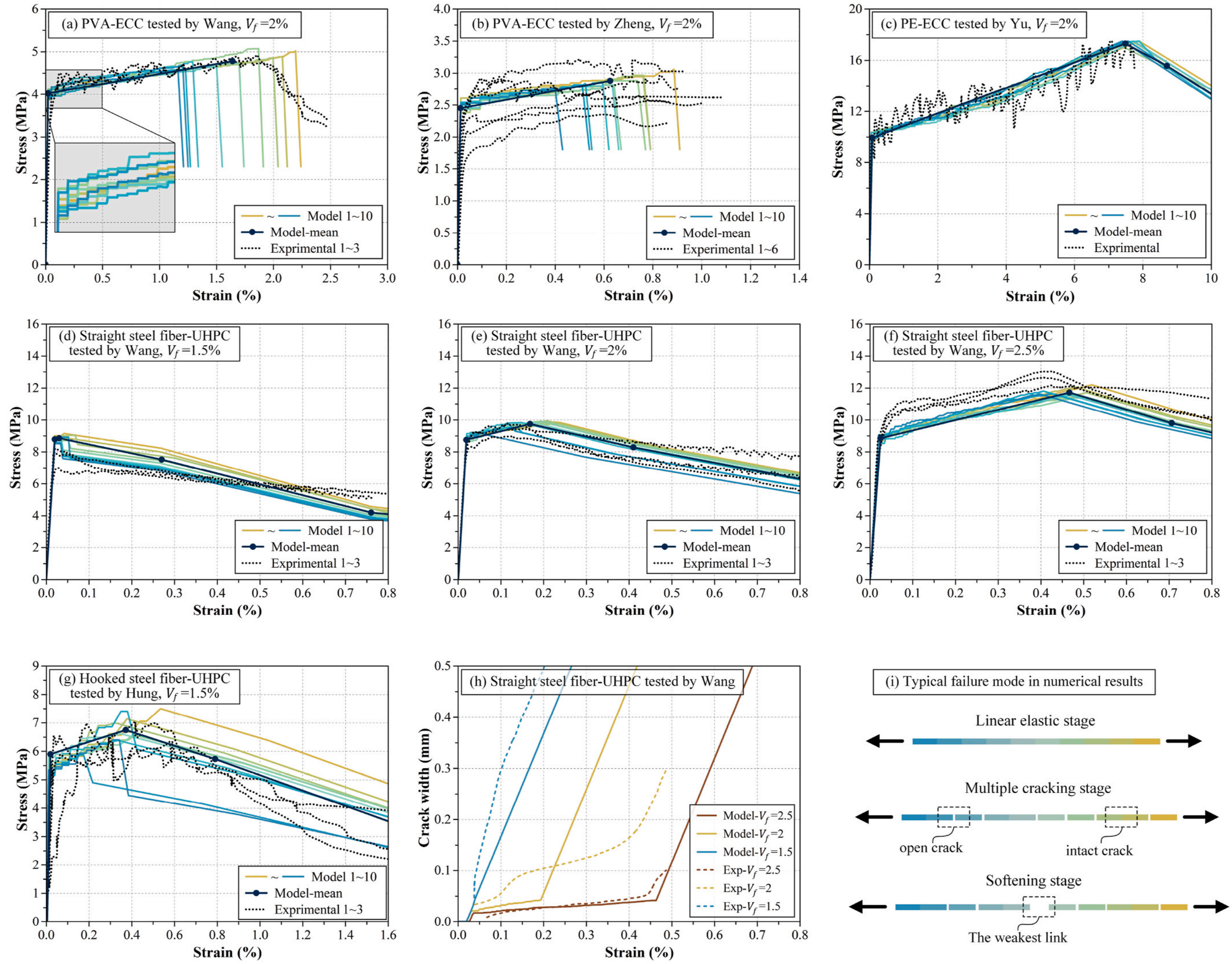

Fig. 8. Tensile stress-strain relationships and crack width-strain curves for PVA-ECC, PE-ECC and UHPC: (a) and (b) the ultimate strength and ductility of PVA-ECC are affected by the physical properties of PVA fibers and stochastic nature; (c) simulations of PE-ECC can be conducted by using the bridging relationship from direct test method; (d)–(g) the volume content and type of steel fibers have a great influence on the tensile behavior of UHPC; (h) and (i) the incorporation of short fibers can constrain the crack width effectively.

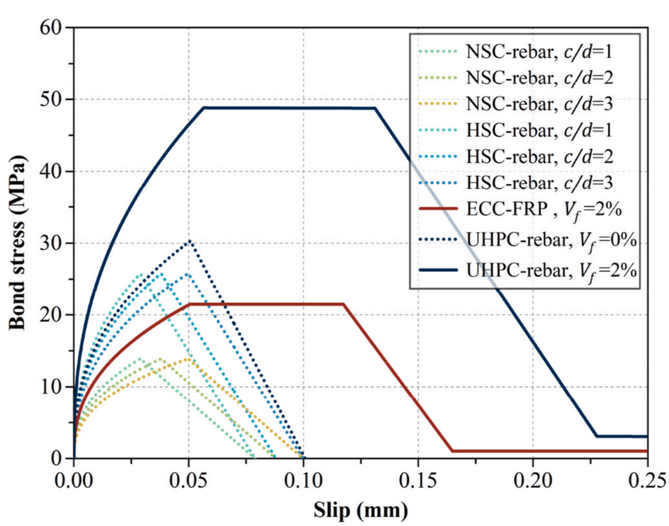

Fig. 9. Local bond-slip laws for the continuous fiber-matrix interface of RC, UHPC-steel and ECC-FRP specimens.

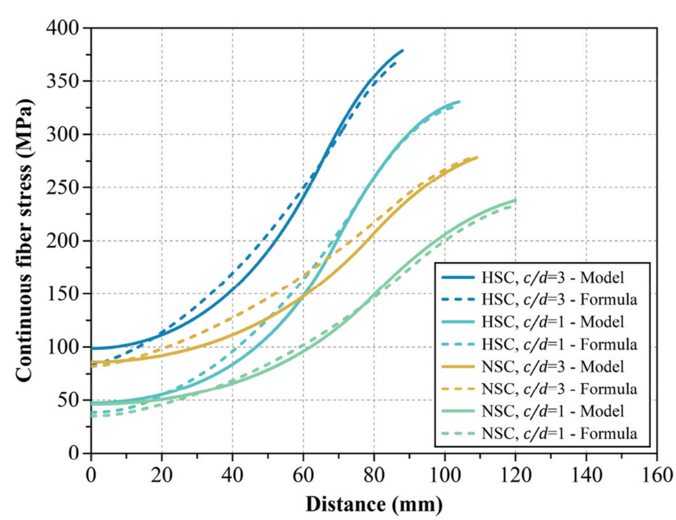

Fig. 10. Stress distribution along the continuous fibers of RC specimens with the specific element length.

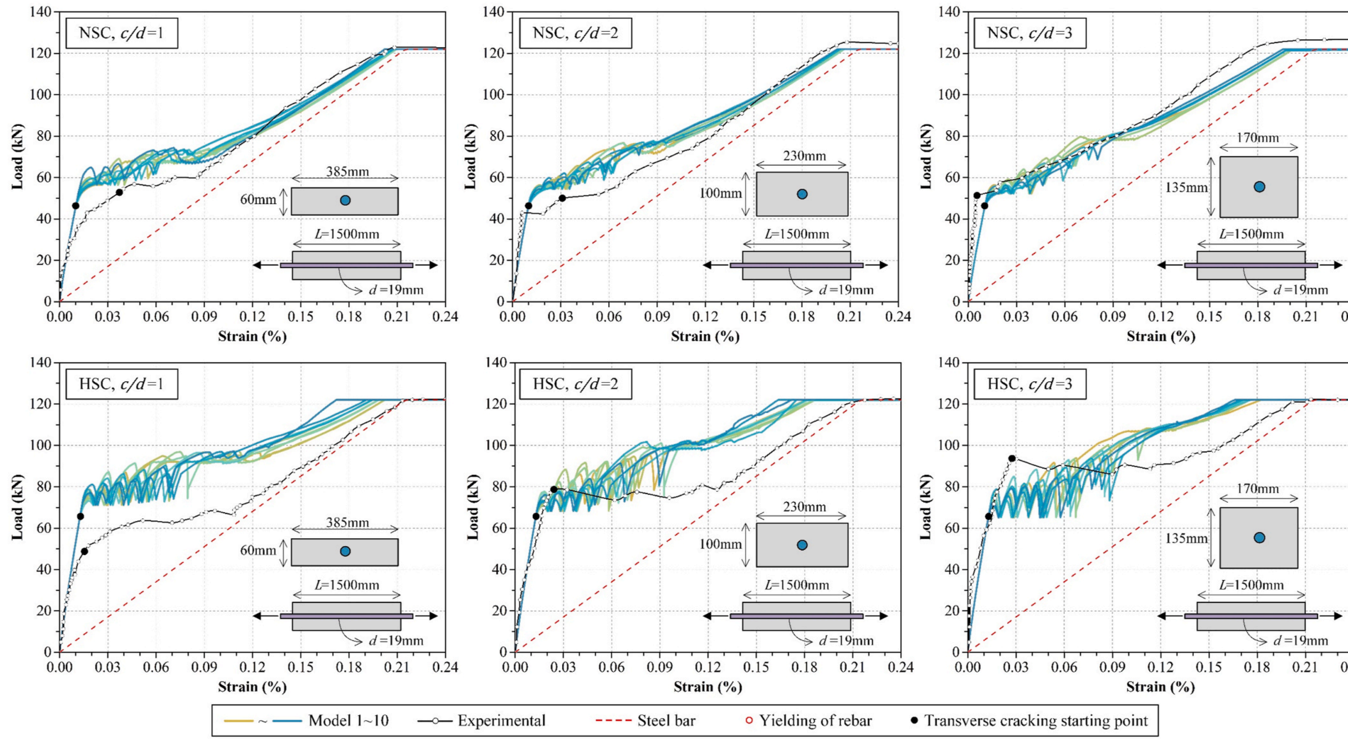

Fig. 11. Initial load-strain curves of the experiments and predictive models for RC with different cover thickness and the compressive strength.

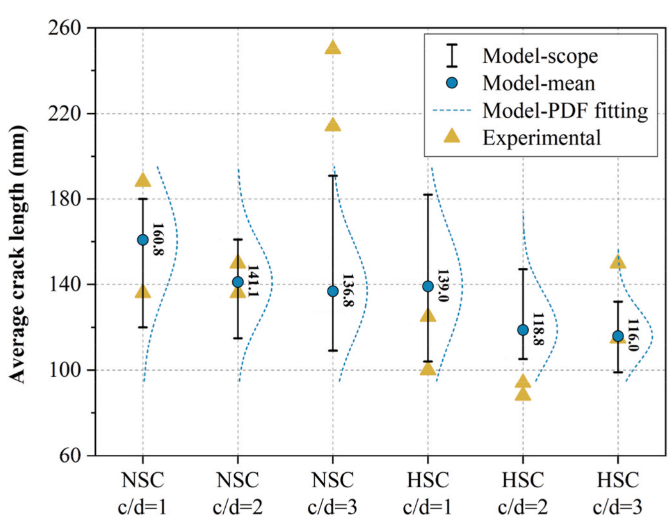

Fig. 12. Average crack spacing of experiments and predictive models for RC.

rupture of FRP at an ultimate strain over 1%. In other words, the ductility enhancing effect can be well captured by the proposed model.

5. Discussion

It is verified that the compatible and universal model can indicate the reinforcing mechanism of fibers at different scales. In terms of the strong variation in existing experiments, the stochastic process and Monte Carlo simulation based on the statistical analysis are conducted in the developed model. The range of simulations can mostly cover the unstable experimental results due to the accurate calibration of stochastic distributions. For chopped short fibers at the mesoscopic scale, the physical properties and fiber-matrix interface behavior can be taken into account by adopting the fiber-bridging constitutive law. For continuous fibers at the macroscopic scale, nonlinear behavior such as rupturing and yielding can be easily considered by defining the constitutive relationship of the truss elements. Furthermore, when $V_r = 0$ or $V_f = 0$, the applicability of the proposed model in the SFRC and CFRC is owing to the subtle correspondence between the bridging stress-COD relationship, local bond-slip law and minimum crack spacing.

Two kinds of springs are used to present different interfacial properties in terms of the composite actions. First, the tension stiffening effect and fiber-bridging model can be characterized by the shear and tensile spring elements, respectively. In addition, the effect of chopped fibers and CNMs on the continuous fiber-matrix interface can be expressed by the bond-slip relationship between CFRC and MSFRC. Finally, the synergetic effect on cracking behavior can be incorporated into the model by the minimum crack spacing derived in this paper.

Overall, the high-precision simulation depends on the adopted bridging law and minimum crack spacing; thus, investigating the influence of nonlinear properties on the cracking behavior is the next step of the study. Meanwhile, the early age autogenous shrinkage [68] and prestress force [69] have a discernible effect on the tensile behavior of MSFRC, for which the developed model can establish a theoretical basis. In addition, because the thin plate is one of the widely applied components in the practical application for MSFRC [18], it is worth considering transforming the 1-D model into 2-D model in terms of the flexural behavior.

6. Conclusions

In this paper, the concept of Multi-Scale Fiber Reinforced Cementitious Composite, abbreviated to MSFRC, is presented. The material is characterized by the tight crack-width control capability, high tensile strength and ductility. The composite actions of MSFRC are analyzed from a universal perspective via a review of previous studies on CFRC and SFRC. Then, the 1-D numerical model based on the crack band theory, fiber-bridging model and stochastic process, is proposed to simulate behaviors of MSFRC. Regarding the discussion throughout this paper, the following conclusions can be summarized.

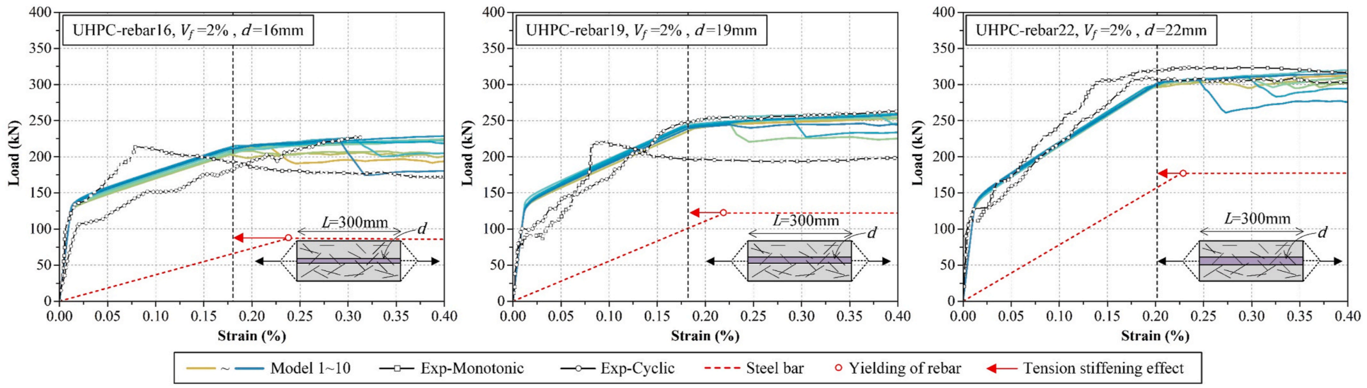

Fig. 13. Initial load-strain curves of the experiments and predictive models for UHPC-rebar with different rebar size: continuous fiber and short fibers can participate in load bearing due to the synergetic effect before steel rebar yields.

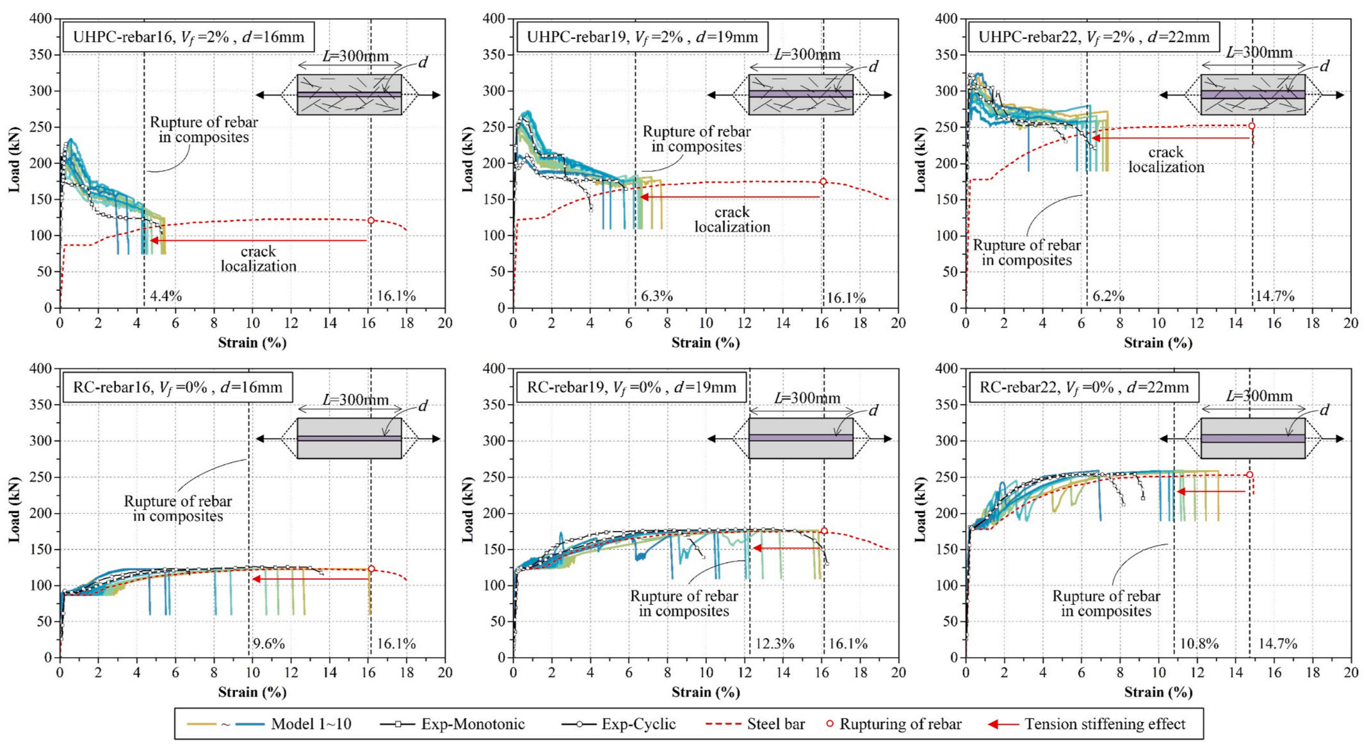

Fig. 14. Complete load-strain curves of experiments and predictive models for UHPC-rebar with different rebar size and short fiber volumetric ratio: peak strength and ultimate strain of UHPC-steel rebar are determined by the physical properties of fibers, and specimens with 2% short fiber volumetric ratio exhibit a lower rupture strain of the rebar than that in the specimens without the incorporation of short fibers.

(1) A model is proposed and developed. In the model, fiber-bridging model and local bond-slip laws are defined and inserted into the interfaces by means of the spring elements. Then, the minimum crack spacing of MSFRC in the model is derived based on the bond-slip behavior and micromechanical-based approach. A fitting method in combination with the probabilistic concept is proposed by using the obtained experimental results to determine the distribution functions of the matrix flaw and fiber dispersion in the absence of statistical data.

(2) The model is proved to be of wide suitability for different materials. It is used in simulations of six independent experiments in terms of the tensile response and crack propagation: PVA-ECC, PE-ECC, UHPC, RC, UHPC-steel rebar and ECC-FRP grid. All simulation results of SFRC, CFRC and MSFRC experiments show good agreement with the experimental results. It is shown that the developed model can take account of the scales, physical properties and volume fractions of reinforcing fibers, interface behavior and stochastic nature.

(3) This model can be used to illuminate the mechanical mechanism and also for material design. In the SFRC cases, the tensile strain-hardening behavior and multiple cracking phenomenon of different SFRC can be simulated, which can be applied to the corresponding MSFRC experiments. In the CFRC case, the validity of the proposed local bond-slip relationship and minimum crack spacing have been demonstrated. In the two cases of MSFRC, the composite actions between cementitious matrix and reinforcing fibers at different scales can be well captured based on the calibrations and validations of SFRC and CFRC. For the synergetic effect, the minimum crack spacing and crack width could be controlled effectively. And, the tension stiffening and ductility enhancing effect are demonstrated to be associated with the fiber

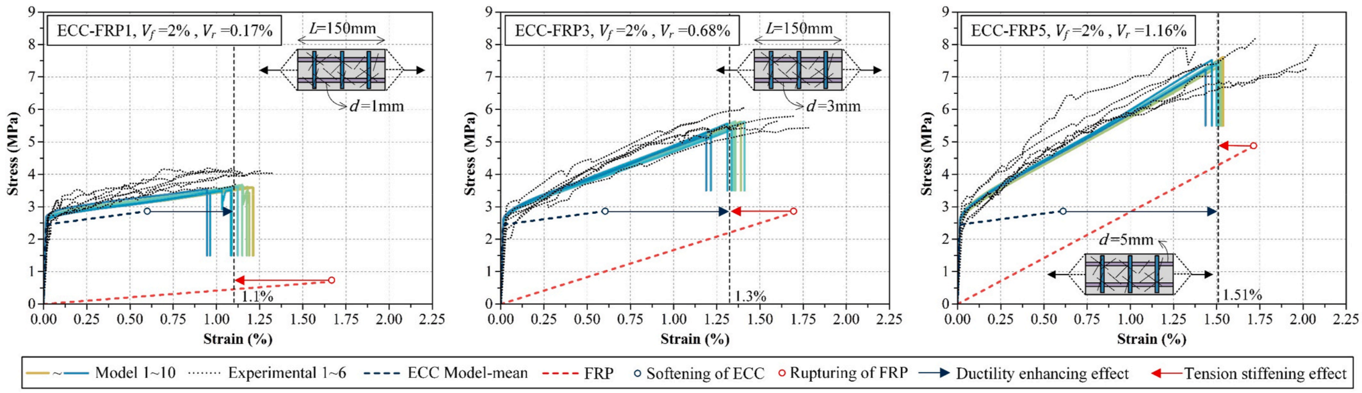

Fig. 15. Stress-strain relationships of the experiments and predictive models for ECC-FRP: FRP grid can exhibit excellent workability with PVA fibers, and the high reinforcement ratio of continuous fiber would lead to a strong synergetic effect.

volume contents and stochastic nature. The above findings and proposed model can facilitate the design of MSFRC.

CRediT authorship contribution statement

Peizhao Zhou: Software, Validation, Formal analysis, Investigation, Data curation, Writing - Original Draft, Visualization. **Peng Feng:** Conceptualization, Methodology, Resources, Writing - Review & Editing, Supervision, Project administration, Funding acquisition.

Declaration of competing interest

The authors declare that they have no known competing financial interests or personal relationships that could have appeared to influence the work reported in this paper.

Data availability

Data will be made available on request.

Acknowledgments

This work was supported by the National Natural Science Foundation of China (No. U2106219) and a grant from the Institute for Guo Qiang, Tsinghua University, China (No. 2021GQI0007).

Appendix A. Calculation of the minimum crack spacing of the strain-hardening SFRC based on the simplified bridging stress-COD relationship

The simplified bridging stress-COD relationship has been presented [6] in terms of the ultimate bridging strength $\sigma_{pb} = V_f L_f \tau_f g/(4r_f)$, the ultimate COD $\delta_{pb} = L_f^2 \tau_f/(2\eta E_f r_f)$, the composite modulus coefficient $\eta = (V_m E_m + V_f E_f)/(V_m E_m)$, the frictional bond strength τ_f, the radius and length of the short fibers r_f and L_f, the elastic modulus of the matrix and short fibers E_m and E_f, and the short fiber volume fraction V_f. In addition, the snubbing factor g can be given as follows:

$$g = 2\int_{\theta=0}^{\frac{\pi}{2}} \int_{z=0}^{\frac{\cos\theta L_f}{2}} e^{f\theta} p(\theta) p(z) dz d\theta \tag{A.1}$$

where $p(\theta)$ and $p(z)$ are the probability density functions of the random fiber orientation and location, $p(z) = 2/L_f$, $p(\theta) = 2/\pi$ for 2D and $p(\theta) = \sin\theta$ for 3D. Then g can be obtained by:

$$g = \begin{cases} \frac{4}{\pi}\frac{e^{\frac{f\pi}{2}} - f}{f^2+1} \ for\ 2D \\ 2\frac{e^{\frac{f\pi}{2}} + 1}{f^2+4} \ for\ 3D \end{cases} \tag{A.2}$$

When the matrix reaches the cracking strength, the crack spacing of strain-hardening SFRC can be derived by the equilibrium condition:

$$F_f + F_{pulley} = \sigma_{mu} V_m \tag{A.3}$$

where F_f is the normal resultant force of the interface friction along the distributed short fiber and F_{pulley} is the resultant pulley force at the end point of the inclined short fibers. Similarly, the equilibrium condition for a single fiber can be obtained by:

$$P_0 \cos\theta + P_{pulley} = P_0 e^{f\theta} \tag{A.4}$$

where P_0 and P_{pulley} are the interface friction and pulley force of a single inclined fiber, respectively. P_0 can be obtained using the crack spacing of SFRC l_f by:

$$P_0 = 2\pi r_f \tau_f l_f \tag{A.5}$$

In addition, the relationship between the resultant force and the force of a single fiber can be established by integrating the contribution of fibers crossing the cross section:

$$F_f = \frac{V_f}{\pi r_f^2}\frac{L_f - l_f}{L_f}\int_{\theta=0}^{\frac{\pi}{2}}\int_{z=0}^{\frac{\cos\theta L_f}{2}} P_0 \cos\theta p(\theta)p(z)dzd\theta \tag{A.6}$$

$$F_{pulley} = \frac{V_f}{\pi r_f^2}\int_{\theta=0}^{\frac{\pi}{2}}\int_{z=0}^{\frac{\cos\theta L_f}{2}} P_{pulley}p(\theta)p(z)dzd\theta \tag{A.7}$$

When the matrix cracks, the released stress will be carried by the bridging force [43]. The equilibrium condition can be given by:

$$\sigma_{mu}V_m = \frac{V_f}{\pi r_f^2}\int_{\theta=0}^{\frac{\pi}{2}}\int_{z=0}^{\frac{\cos\theta L_f}{2}} P_0 e^{f\theta}p(\theta)p(z)dzd\theta \tag{A.8}$$

Substituting Eq. (A.5) into (A.6), Eqs. (A.4) and (A.8) into (A.7), respectively, F_{pulley} and F_f can be expressed as follows:

$$F_f = \frac{V_f \tau_f l_f (L_f - l_f)\lambda_\theta}{r_f L_f} \tag{A.9}$$

$$F_{pulley} = \sigma_{mu}V_m\left(1 - \frac{\lambda_\theta}{g}\right) \tag{A.10}$$

where $\lambda_\theta = 1$ for a 2-D uniform distribution and $\lambda_\theta = 2/3$ for a 3-D uniform distribution. Combining Eqs. (A.3), (A.9) and (A.10), l_f can be expressed in Ref. [43] as:

$$l_f = \frac{L_f - \sqrt{L_f^2 - 4L_f l_f'}}{2} \tag{A.11}$$

where $l_f' = \sigma_{mu}V_m r_f/(gV_f\tau_f)$ is defined as the transmission length of short fibers.

Appendix B. Calculation of the average bond stress along the minimum crack spacing by the local bond-slip relationship

For CFRC, the mechanical model of the continuous fiber reinforced brittle matrix subjected to a pull-out force P is shown in Fig. B.1. P is parallel to the fiber axis and can be expressed by the normal stress σ_{rl} of the continuous fiber at the loaded end as follows:

$$P = \pi r_r^2 \sigma_{rl} \tag{B.1}$$

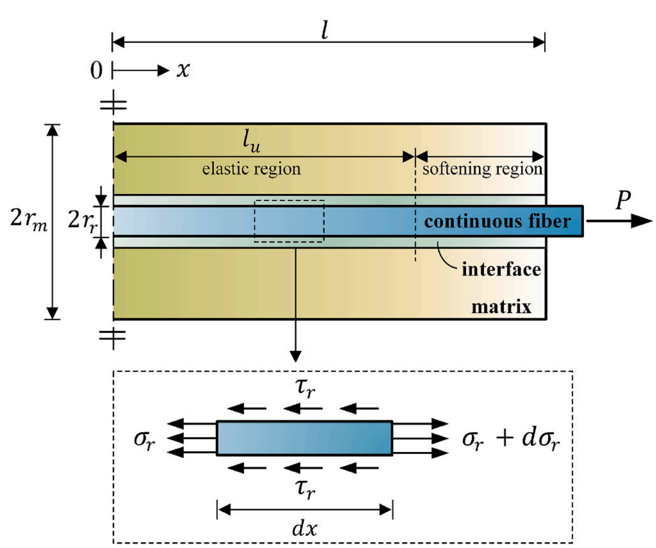

Fig. B.1. The pull-out model of the continuous fiber from matrix.

The embedment length of the continuous fiber is l. Both the fiber and matrix are assumed to behave in isotropic and elastic states with moduli of E_r and E_m, respectively. For a segment of the continuous fiber with a length of dx, the relationship between the tensile normal stress σ_r and the interfacial shear stress τ_r can be derived according to the equilibrium condition of forces:

$$\tau_r = \frac{r_r}{2}\frac{d\sigma_r}{dx} \tag{B.2}$$

where u_r and u_m are the axial displacements of the fiber and matrix at the same location. Then differentiating the shear sliding s between them with respect to x shows the following:

$$\frac{ds}{dx} = \frac{du_r}{dx} - \frac{du_m}{dx} = \frac{\sigma_r}{E_r} - \frac{\sigma_m}{E_m} \tag{B.3}$$

The equilibrium equation including the axial tensile force and normal stress, can be established as:

$$P = \pi\left(r_m^2 - r_r^2\right)\sigma_m + \pi r_r^2 \sigma_r \tag{B.4}$$

where $r_m = \sqrt{A/\pi}$. Then, the normal stress σ_m of the matrix can be derived by:

$$\sigma_m = \frac{(\sigma_{rl} - \sigma_r) r_r^2}{\left(r_m^2 - r_r^2\right)} \tag{B.5}$$

However, the 0.4 power of the rising branch in Eq. (19a) increases the difficulty of solving the governing differential equation. Thus, based on the interfacial energy balance approach, the nonlinear local bond-slip law is simplified to a linear envelope by modifying the transferable load τ_{ue}:

$$\tau = \begin{cases} k_\alpha s \quad (s \le s_u) & \text{(B.6a)} \\ k_\beta (s_{max} - s) \quad (s_u < s \le s_{max}) & \text{(B.6b)} \end{cases}$$

Herein, $k_\alpha = \frac{\tau_{ue}}{s_u}$; $k_\beta = \tau_{ue}/(s_{max} - s_u)$; and $\tau_{ue} = (0.429 s_u / s_{max} + 1)\tau_u$.

When the interface behaves in the elastic state, by combining Eqs.(B.2), (B.3), (B.4) and (B.6a), the governing differential equation is obtained as:

$$\frac{d^2\sigma_r}{dx^2} - \alpha_1^2 \sigma_r + \alpha_2 \sigma_{rl} = 0 \tag{B.7}$$

where

$$\alpha_1^2 = \frac{2k_\alpha}{r_r}\left(\frac{1}{E_r} + \frac{r_r^2}{E_m\left(r_m^2 - r_r^2\right)}\right) \tag{B.8}$$

$$= \frac{2k_\alpha r_r}{E_m\left(r_m^2 - r_r^2\right)} \tag{B.9}$$

The analytical solution of Eqn. (B.7) can be derived as:

$$\sigma_r(x) = C_1 \cosh(\alpha_1 x) + C_2 \sinh(\alpha_1 x) + \frac{\alpha_2}{\alpha_1^2}\sigma_{rl} \tag{B.10}$$

$$\tau_r(x) = \frac{r_r \alpha_1}{2}\left(C_1 \sinh(\alpha_1 x) + C_2 \cosh(\alpha_1 x)\right) \tag{B.11}$$

By applying the boundary conditions $\sigma_r(l) = \sigma_{rl}$ and $\tau_r(0) = 0$, C_1 and C_2 can be determined as:

$$C_1 = \left(1 - \frac{\alpha_2}{\alpha_1^2}\right)\frac{\sigma_{rl}}{\cosh(\alpha_1 l)} \quad C_2 = 0 \tag{B.12}$$

Then, the analytical solution for the elastic stage of the bond-slip relationship becomes:

$$\sigma_r(x) = \sigma_{rl}\left[\left(1 - \frac{\alpha_2}{\alpha_1^2}\right)\frac{\cosh(\alpha_1 x)}{\cosh(\alpha_1 l)} + \frac{\alpha_2}{\alpha_1^2}\right] \tag{B.13}$$

$$\tau_r(x) = \frac{r_r}{2}\alpha_1 \sigma_{rl}\left(1 - \frac{\alpha_2}{\alpha_1^2}\right)\frac{\sinh(\alpha_1 x)}{\cosh(\alpha_1 l)} \tag{B.14}$$

Once the slip of the interface exceeds s_u, the region along the length l can be divided into the elastic region ($0 \le x < l_u$) and softening region ($l_u \le x < l$), where l_u is the damage propagation length.

For the elastic region ($0 \le x < l_u$), the analytical solution can be derived by replacing l and σ_{rl} with l_u and the normal stress σ_{rlu} at $x = l_u$, respectively. Furthermore, by applying the new boundary condition, i.e., $\tau(0) = 0$, $\tau(l_u) = \tau_{ue}$ and $\sigma_r(l_u) = \sigma_{rlu}$ to the solution, we have:

$$\sigma_r(lu) = \sigma_{rlu} = \frac{2\tau_{ue}}{r_r \alpha_1\left(1 - \frac{\alpha_2}{\alpha_1^2}\right)\tanh(\alpha_1 l_u)} \tag{B.15}$$

$$\sigma_r(0) = \sigma_{r0} = \sigma_{rlu}\left[\left(1-\frac{\alpha_2}{\alpha_1^2}\right)\frac{1}{\cosh(\alpha_1 l_u)}+\frac{\alpha_2}{\alpha_1^2}\right] \tag{B.16}$$

For the softening region ($l_u \le x < l$), the governing differential equation Eqn. (B.7) is rewritten by replacing the dominated relationship as follows:

$$\frac{d^2\sigma_r}{dx^2}+\beta_1^2\sigma_r-\beta_2\sigma_{rl}=0 \tag{B.17}$$

where

$$\beta_1^2=\frac{2k_\beta}{r_r}\left(\frac{1}{E_r}+\frac{r_r^2}{E_m\left(r_m^2-r_r^2\right)}\right) \tag{B.18}$$

$$\beta_2=\frac{2k_\beta r_r}{E_m\left(r_m^2-r_r^2\right)} \tag{B.19}$$

The analytical solution of Eq.(B.17) can be derived as:

$$\sigma_r(x)=C_3\cos(\beta_1 x)+C_4\sin(\beta_1 x)+\frac{\beta_2}{\beta_1^2}\sigma_{rl} \tag{B.20}$$

Herein, C_3 and C_4 can be determined by adopting the boundary conditions, i.e., $\sigma_r(l_u)=\sigma_{rlu}$ and $\tau_r(l_u)=\tau_{ue}$:

$$\begin{aligned} C_3 &= \sigma_{rlu}\,cos(\beta_1 l_u)-\frac{\beta_2}{\beta_1^2}\sigma_{rl}\,cos(\beta_1 l_u)-\frac{2\tau_{ue}\,sin(\beta_1 l_u)}{\beta_1 r_r} \\ C_4 &= \sigma_{rlu}\,sin(\beta_1 l_u)-\frac{\beta_2}{\beta_1^2}\sigma_{rl}\,sin(\beta_1 l_u)+\frac{2\tau_{ue}\,cos(\beta_1 l_u)}{\beta_1 r_r} \end{aligned} \tag{B.21}$$

The normal stress $\sigma_r(l)$ of the continuous fiber at $x = l$, written as σ_{rl}, is obtained as:

$$\sigma_{rl}=\frac{\left\{\begin{array}{l}\sigma_{rlu}[\cos(\beta_1 l_u)\cos(\beta_1 l)+\sin(\beta_1 l_u)\sin(\beta_1 l)]+\\ \dfrac{2\tau_{ue}}{\beta_1 r_r}[sin(\beta_1 l)cos(\beta_1 l_u)-sin(\beta_1 l_u)cos(\beta_1 l)]\end{array}\right\}}{\left[1-\dfrac{\beta_2}{\beta_1^2}+\dfrac{\beta_2}{\beta_1^2}cos(\beta_1 l_u)cos(\beta_1 l)+\dfrac{\beta_2}{\beta_1^2}sin(\beta_1 l_u)sin(\beta_1 l)\right]} \tag{B.22}$$

σ_{r0} and σ_{rl} can be expressed as the functions, $\sigma_{r0}(l_u)$ and $\sigma_{rl}(l_u)$, because l_u is the variable during loading. The force transferred from the continuous fiber to the matrix can be written as:

$$P_{bs}(l_u)=\pi r_r^2[\sigma_{rl}(l_u)-\sigma_{r0}(l_u)] \tag{B.23}$$

By solving $dP_{bs}(l_u)/dl_u = 0$, the critical damage propagation length l_{uc} is derived, and the critical average bond strength can be written as:

$$\overline{\tau_r}=\frac{[\sigma_{rl}(l_{uc})-\sigma_{r0}(l_{uc})]r_r}{2l} \tag{B.24}$$

References

[1] Bažant ZP, Oh BH. Crack band theory for fracture of concrete. Matériaux et Const. 1983;16:155–77.
[2] Xu S, Liu J, Li Q. Mechanical properties and microstructure of multi-walled carbon nanotube-reinforced cement paste. Construct Build Mater 2015;76:16–23.
[3] Li VC, Obla KH. Effect of fiber length variation on tensile properties of carbon-fiber cement composites. Compos Eng 1994;4:947–64.
[4] Yang E-H, Li VC. Strain-hardening fiber cement optimization and component tailoring by means of a micromechanical model. Construct Build Mater 2010;24:130–9.
[5] Oh T, You I, Banthia N, Yoo D-Y. Deposition of nanosilica particles on fiber surface for improving interfacial bond and tensile performances of ultra-high-performance. Compos B Eng 2021:221.
[6] Li VC, Leung CKY. Steady-state and multiple cracking of short random fiber composites. J Eng Mech-Asce 1992;118:2246–64.
[7] Lu C, Leung CKY, Li VC. Numerical model on the stress field and multiple cracking behavior of Engineered Cementitious Composites (ECC). Construct Build Mater 2017;133:118–27.
[8] Chen YL, Liu B, He XQ, Huang Y, Hwang KC. Failure analysis and the optimal toughness design of carbon nanotube-reinforced composites. Compos Sci Technol 2010;70:1360–7.
[9] Quinteros L, García-Macías E, Martínez-Pañeda E. Micromechanics-based phase field fracture modelling of CNT composites. Compos B Eng 2022:236.
[10] Ahmed HU, Faraj RH, Hilal N, Mohammed AA, Sherwani AFH. Use of recycled fibers in concrete composites: a systematic comprehensive review. Compos B Eng 2021:215.
[11] Xu L-Y, Nie X, Zhou M, Tao M-X. Whole-process crack width prediction of reinforced concrete structures considering bonding deterioration. Eng Struct 2017;142:240–54.
[12] Triantafyllou GG, Rousakis TC, Karabinis AI. Analytical assessment of the bearing capacity of RC beams with corroded steel bars beyond concrete cover cracking. Compos B Eng 2017;119:132–40.
[13] Du J, Meng W, Khayat KH, Bao Y, Guo P, Lyu Z, et al. New development of ultra-high-performance concrete (UHPC). Compos B Eng 2021:224.
[14] Gong J, Ma Y, Fu J, Hu J, Ouyang X, Zhang Z, Wang H. Utilization of fibers in ultra-high performance concrete: a review. Compos B Eng 2022:241.
[15] Wang S, Yu L, Yang F, Xu L, Wu K, De Schutter G, Yang Z. Effect of steel fiber distribution on the mechanical properties of UHPC caused by vehicle-bridge coupling vibration. Compos B Eng 2022:245.
[16] Zhang H, Wu Z, Hu X, Ouyang X, Zhang Z, Banthia N, Shi C. Design, production, and properties of high-strength high-ductility cementitious composite (HSHDCC): a review. Compos B Eng 2022:247.
[17] Zheng Y-Z, Wang W-W, Brigham JC. Flexural behaviour of reinforced concrete beams strengthened with a composite reinforcement layer: BFRP grid and ECC. Construct Build Mater 2016;115:424–37.
[18] Ye Y-Y, Smith ST, Zeng J-J, Zhuge Y, Quach W-M. Novel ultra-high-performance concrete composite plates reinforced with FRP grid: development and mechanical behaviour. Compos Struct 2021:269.

[19] Meng W, Khayat KH, Bao Y. Flexural behaviors of fiber-reinforced polymer fabric reinforced ultra-high-performance concrete panels. Cement Concr Compos 2018;93:43–53.
[20] Zheng Y-Z, Wang W-W, Mosalam KM, Zhu Z-F. Mechanical behavior of ultra-high toughness cementitious composite strengthened with Fiber Reinforced Polymer grid. Compos Struct 2018;184:1–10.
[21] Li B, Xiong H, Jiang J, Dou X. Tensile behavior of basalt textile grid reinforced Engineering Cementitious Composite. Compos B Eng 2019;156:185–200.
[22] Gong T, Ahmed AH, Curosu I, Mechtcherine V. Tensile behavior of hybrid fiber reinforced composites made of strain-hardening cement-based composites (SHCC) and carbon textile. Construct Build Mater 2020:262.
[23] Fischer G, Li VC. Influence of matrix ductility on tension-stiffening behavior of steel reinforced engineered cementitious composites (ECC). Struct J 2002;99:104–11.
[24] Kang S-B, Tan KH, Zhou X-H, Yang B. Influence of reinforcement ratio on tension stiffening of reinforced engineered cementitious composites. Eng Struct 2017;141:251–62.
[25]] Mündecke E, Mechtcherine V. Tensile behaviour of strain-hardening cement-based composites (SHCC) with steel reinforcing bars. Cement Concr Compos 2020;105.
[26] Hung C-C, Lee H-S, Chan SN. Tension-stiffening effect in steel-reinforced UHPC composites: constitutive model and effects of steel fibers, loading patterns, and rebar sizes. Compos B Eng 2019;158:269–78.
[27] Lee S-C, Cho J-Y, Vecchio FJ. Tension-stiffening model for steel fiber-reinforced concrete containing conventional reinforcement. ACI Struct J 2013;110.
[28] Deluce JR, Lee S-C, Vecchio FJ. Crack model for steel fiber-reinforced concrete members containing conventional reinforcement. ACI Struct J 2014;111:93.
[29] Chen C, Cai H, Li J, Zhong P, Huang B, Sui L, Zhou Y. One-dimensional extended FEM based approach for predicting the tensile behavior of SHCC-FRP composites. Engineering Fracture Mechanics; 2019.
[30] Aveston J, Kelly A. Theory of multiple fracture of fibrous composites. J Mater Sci 1973;8:352–62.
[31] Curtin WA, Ahn BK, Takeda N. Modeling brittle and tough stress–strain behavior in unidirectional ceramic matrix composites. Acta Mater 1998;46:3409–20.
[32] Hegger J, Will N, Bruckermann O, Voss S. Load–bearing behaviour and simulation of textile reinforced concrete. Mater Struct 2006;39:765–76.
[33] Misseri G, Rovero L, Galassi S. Analytical modelling bond behaviour of polybenzoxazole (PBO) and glass Fibre Reinforced Cementitious Matrix (FRCM) systems coupled with cement and gypsum matrixes: effect of the Cohesive Material Law (CML) shape. Compos B Eng 2021:223.
[34] Mu-xuan T, Ji-zhi Z. Predicting the crack width of reinforced concrete structural members using the smeared crack model and layered shell elements in general-purpose finite element packages. Eng Mech 2020;37:165–77.
[35] Pulatsu B, Erdogmus E, Lourenço PB, Lemos JV, Tuncay K. Numerical modeling of the tension stiffening in reinforced concrete members via discontinuum models. Comput Part Mech 2020;8:423–36.
[36] Asim N, Badiei M, Samsudin NA, Mohammad M, Razali H, Soltani S, Amin N. Application of graphene-based materials in developing sustainable infrastructure: an overview. Compos B Eng 2022:245.
[37] Wang W, Chen SJ, Sagoe-Crentsil K, Duan W. Graphene oxide-reinforced thin shells for high-performance, lightweight cement composites. Compos B Eng 2022:235.
[38] Meng T, Ying K, Yu H, Hong Y. An approach to effectively improve the interfacial bonding of paste–limestone by incorporating different nanomaterials. Compos B Eng 2022:242.
[39] Slobbe AT, Hendriks MAN, Rots JG. Systematic assessment of directional mesh bias with periodic boundary conditions: applied to the crack band model. Eng Fract Mech 2013;109:186–208.
[40] Wang S. Micromechanics based matrix design for engineered cementitious composites. University of Michigan; 2005.
[41] Li Y, Ruan X, Akiyama M, Zhang M, Xin J, Lim S. Modelling method of fibre distribution in steel fibre reinforced concrete based on X-ray image recognition. Compos B Eng 2021:223.
[42] Junxia L, Weng J, Yang E-H. Stochastic model of tensile behavior of strain-hardening cementitious composites (SHCCs). Cement Concr Res 2019:124.
[43] Lu C, Leung CKY. A new model for the cracking process and tensile ductility of Strain Hardening Cementitious Composites (SHCC). Cement Concr Res 2016;79:353–65.
[44] Huang T, Zhang YX. Numerical modelling of mechanical behaviour of engineered cementitious composites under axial tension. Comput Struct 2016;173:95–108.
[45] Kanda T, Lin Z, Li VC. Tensile stress-strain modeling of pseudostrain hardening cementitious composites. J Mater Civ Eng 2000;12:147–56.
[46] Fischer G, Li VC. Effect of fiber reinforcement on the response of structural members. Eng Fract Mech 2007;74:258–72.
[47] Wang X, Ding S, Qiu L, Ashour A, Wang Y, Han B, Ou J. Improving bond of fiber-reinforced polymer bars with concrete through incorporating nanomaterials. Compos B Eng 2022:239.
[48] Lu S, Xia W, Bai E, Ling L, Du Y. Interfacial modification: the dynamic compression properties and enhancement mechanism of concrete added with micro-nano hierarchical carbon-based fiber. Compos B Eng 2022:247.
[49] Dancygier AN, Berkover E. Cracking localization and reduced ductility in fiber-reinforced concrete beams with low reinforcement ratios. Eng Struct 2016;111:411–24.
[50] Zhang J, Ju X. Investigation on stress-crack opening relationship of engineered cementitious composites using inverse approach. Cement Concr Res 2011;41:903–12.
[51] Xie C, Cao M, Guan J, Liu Z, Khan M. Improvement of boundary effect model in multi-scale hybrid fibers reinforced cementitious composite and prediction of its structural failure behavior. Compos B Eng 2021:224.
[52] GB. Code for design of concrete structures. Beijing: China Building Industry Press; 2010, 50010 [in Chinese].
[53] Esmaeily A, Xiao Y. Behavior of reinforced concrete columns under variable axial loads: analysis. ACI Struct J 2005;102:736.
[54] Haskett M, Oehlers DJ, Mohamed Ali MS. Local and global bond characteristics of steel reinforcing bars. Eng Struct 2008;30:376–83.
[55] Lin H, Zhao Y, Ozbolt J, Feng P, Jiang C, Eligehausen R. Analytical model for the bond stress-slip relationship of deformed bars in normal strength concrete. Construct Build Mater 2019;198:570–86.
[56] Mirza SM, Houde J. Study of bond stress-slip relationships in reinforced concrete. J Proc 1979:19–46.
[57] Gan Y. Bond stress and slip modeling in nonlinear finite element analysis of reinforced concrete structures. University of Toronto; 2000.
[58] Bažant ZP, Li Z, Thoma M. Identification of stress-slip law for bar or fiber pullout by size effect tests. J Eng Mech 1995;121:620–5.
[59] Harajli M, Hamad B, Karam K. Bond-slip response of reinforcing bars embedded in plain and fiber concrete. J Mater Civ Eng 2002;14:503–11.
[60] Lee G-Y, Kim W. Cracking and tension stiffening behavior of high-strength concrete tension members subjected to axial load. Adv Struct Eng 2008;12:127–37.
[61] Lam L, Wong Y, Poon C-S. Effect of fly ash and silica fume on compressive and fracture behaviors of concrete. Cement Concr Res 1998;28:271–83.
[62] Huang T, Zhang YX, Su C, Lo SR. Effect of slip-hardening interface behavior on fiber rupture and crack bridging in fiber-reinforced cementitious composites. J Eng Mech 2015:141.
[63] Wang J-Y, Guo J-Y. Damage investigation of ultra high performance concrete under direct tensile test using acoustic emission techniques. Cement Concr Compos 2018;88:17–28.
[64] Yoo D-Y, Park J-J, Kim S-W. Fiber pullout behavior of HPFRCC: effects of matrix strength and fiber type. Compos Struct 2017;174:263–76.
[65] Lee Y, Kang S-T, Kim J-K. Pullout behavior of inclined steel fiber in an ultra-high strength cementitious matrix. Construct Build Mater 2010;24:2030–41.
[66] Ahmad S, Mohaisen KO, Adekunle SK, Al-Dulaijan SU, Maslehuddin M. Influence of admixing natural pozzolan as partial replacement of cement and microsilica in UHPC mixtures. Construct Build Mater 2019;198:437–44.
[67] Yu K-Q, Lu Z-D, Dai J-G, Shah SP. Direct tensile properties and stress–strain model of UHP-ECC. J Mater Civ Eng 2020;32.
[68] Yoo D-Y, Park J-J, Kim S-W, Yoon Y-S. Influence of reinforcing bar type on autogenous shrinkage stress and bond behavior of ultra high performance fiber reinforced concrete. Cement Concr Compos 2014;48:150–61.
[69] Zhu D, Liu S, Yao Y, Li G, Du Y, Shi C. Effects of short fiber and pre-tension on the tensile behavior of basalt textile reinforced concrete. Cement Concr Compos 2019;96:33–45.